IMPURITY ABSORPTION SPECTROSCOPY OF THE DEEP DOUBLE DONOR SULFUR IN ISOTOPICALLY ENRICHED SILICON

by

Michael Steger
Vordiplom, Universität Augsburg, Germany, 2003

A THESIS SUBMITTED IN PARTIAL FULFILLMENT
OF THE REQUIREMENTS FOR THE DEGREE OF
MASTER OF SCIENCE
in the Department
of
Physics

SIMON FRASER UNIVERSITY
2007

APPROVAL

Name:	Michael Steger
Degree:	Master of Science
Title of thesis:	Impurity Absorption Spectroscopy of the Deep Double Donor Sulfur in Isotopically Enriched Silicon

Examining Committee: Dr. Karen Kavanagh, Professor
Chair

Dr. Michael L. W. Thewalt, Professor
Senior Supervisor

Dr. Simon P. Watkins, Professor
Supervisor

Dr. Patricia M. Mooney, Professor
Supervisor

Dr. George Kirczenow, Professor
Internal Examiner

Date Approved: July 18, 2007

SFU SIMON FRASER UNIVERSITY
LIBRARY

Declaration of Partial Copyright Licence

The author, whose copyright is declared on the title page of this work, has granted to Simon Fraser University the right to lend this thesis, project or extended essay to users of the Simon Fraser University Library, and to make partial or single copies only for such users or in response to a request from the library of any other university, or other educational institution, on its own behalf or for one of its users.

The author has further granted permission to Simon Fraser University to keep or make a digital copy for use in its circulating collection (currently available to the public at the "Institutional Repository" link of the SFU Library website <www.lib.sfu.ca> at: <http://ir.lib.sfu.ca/handle/1892/112>) and, without changing the content, to translate the thesis/project or extended essays, if technically possible, to any medium or format for the purpose of preservation of the digital work.

The author has further agreed that permission for multiple copying of this work for scholarly purposes may be granted by either the author or the Dean of Graduate Studies.

It is understood that copying or publication of this work for financial gain shall not be allowed without the author's written permission.

Permission for public performance, or limited permission for private scholarly use, of any multimedia materials forming part of this work, may have been granted by the author. This information may be found on the separately catalogued multimedia material and in the signed Partial Copyright Licence.

While licensing SFU to permit the above uses, the author retains copyright in the thesis, project or extended essays, including the right to change the work for subsequent purposes, including editing and publishing the work in whole or in part, and licensing other parties, as the author may desire.

The original Partial Copyright Licence attesting to these terms, and signed by this author, may be found in the original bound copy of this work, retained in the Simon Fraser University Archive.

Simon Fraser University Library
Burnaby, BC, Canada

Revised: Summer 2007

Abstract

The chalcogen deep double donor sulfur in natural silicon ($^{\mathrm{nat}}$Si) has been studied extensively with optical methods in the past. Recently it was shown that the spectroscopic linewidth of shallow impurity absorption transitions is limited by inhomogeneous broadening due to a silicon isotope effect which is removed by the use of highly enriched ^{28}Si. In this work we extend these results to deep centres. Several different samples were prepared, allowing for a systematic identification of isotope effects. The observed isotope effects include the elimination of inhomogeneous broadening, energy shifts and the removal of satellite peaks. The S^+ $1s(T_2)$ transition exhibits a width of only $0.008\,\mathrm{cm}^{-1}$ for the Γ_7 component – more than one order of magnitude sharper than in $^{\mathrm{nat}}$Si and less than a quarter the width of the sharpest phosphorus transition in ^{28}Si. It is the narrowest optical transition ever seen for impurity states in silicon.

für Opa

Acknowledgments

First and foremost I would like to thank my Senior Supervisor Dr. Michael Thewalt for accepting me into his research group. His vast knowledge, his intuitive experimental skills and his excitement for science were an invaluable help and guidance for this work.

Furthermore I acknowledge Albion Yang for helpful discussions and for being a great colleague and friend.

This project would not have been possible without the sample material provided by the Avogadro Project and Eugene E. Haller.

For generous financial support I would like to acknowledge Dr. Michael Thewalt and the Department of Physics, Simon Fraser University.

And last but not least I am especially thankful to my father Maximilian – you are the greatest – and to Garima.

Contents

List of Tables

List of Figures

Chapter 1

Introduction

1.1 Isotopically enriched silicon

There has been increasing interest in the properties of materials enriched in the stable isotopes of silicon. It has been found that photoluminescence and impurity absorption lines in isotopically enriched silicon are extraordinarily sharp and reveal previously unseen effects.

In early spectroscopic studies of impurity centres in silicon, the widths of infrared absorption lines resulting from transitions between the electronic ground state and a bound excited state of the impurity centre were dominated by inhomogeneous fields and inter-impurity interactions as a consequence of high impurity concentrations and imperfect crystals. Progress was made in controlling the crystalline perfection and the chemical purity of silicon single crystals, reducing the line width of absorption transitions. The quality of the Si samples came to a point where no significant improvement in linewidth was observed. This result suggested that a fundamental lifetime broadening limit had been found and that all inhomogeneous broadening effects were eliminated. Barrie and Nishikawa [1, 2] proposed that this lifetime broadening was a result of phonon-assisted transitions from the excited state to other near-lying states. This mechanism was in reasonable agreement with the observed linewidths in high quality samples until recently, and was thus assumed to be the limiting factor.

The advent of isotopically enriched silicon immediately showed that the isotopic composition and isotopic randomness of the host material has a strong influence on the observed linewidth of absorption transitions.

The elimination of inhomogeneous broadening due to isotope effects in silicon was first observed by Karaiskaj et al. [3] in highly enriched ^{28}Si. It was shown that the limiting factor of the linewidth of no-phonon bound exciton photoluminescence transitions in high purity silicon are local fluctuations in the band gap due to isotopic randomness. The observed photoluminescence linewidths were much narrower than previously reported [4] and limited by the instrumental resolution. This experimental limitation has recently been lifted with the introduction of the photoluminescence excitation (PLE) method [5, 6]. Later it was also shown [7] that the isotopic randomness present in Si produces a significant inhomogeneous broadening of many of the already thoroughly studied ground state to excited state infrared absorption transitions of shallow donors and acceptors. Thus, many of these transitions are much sharper in isotopically pure Si than in natural Si, and many of the homogeneous linewidths are much narrower than had been previously assumed. It was also shown [8] that the impurity binding energy depends on the host isotope mass. Thus, depending on which isotope is enriched in the host material, absorption lines appear at slightly different energies. Another consequence is that an impurity centre can have a varying binding energy whenever the average host isotope mass in its vicinity is different from the average isotopic composition of the host material. For phosphorus and boron impurity centres this is believed to cause both broadenings and tails on the absorption lines [9].

Also in [7] it was shown for boron that the isotopic composition of the impurity can cause an energy splitting of the transition, resulting from a dependence of the ground state binding energy on the impurity isotopic mass. This splitting is only visible because of the significantly narrower linewidths of the boron absorption lines in ^{28}Si. The intensity ratios of the split lines correspond to the abundance of the different impurity isotopes.

1.2 The experiment

Much work has been done in the past on the spectroscopy of sulfur doped natural silicon [10–14]. Absorption spectra are a valuable source of information about such centres. High quality absorption spectra can reveal details about the microscopic structure of defect centres. As we know now the advent of isotopically enriched silicon as a host material promises to give us a deeper, more accurate insight into the physics of impurity centres.

By using this new host material, isotopically enriched ^{28}Si and ^{30}Si together with two different isotopic compositions of the deep centre sulfur, $^{\mathrm{nat}}$S (essentially ^{32}S) and ^{34}S, we expect to observe similar effects as the previously mentioned ones for boron and phosphorous. First and foremost this will be a reduction of the full width at half maximum (FWHM) of many (but not all) absorption lines. As a result some phenomena will be more clearly resolved in the spectra. The random placement of different isotopes in the close vicinity of the impurity centre causes satellite peaks for the S^+ $1s(T_2)$ transition [11]. It is expected that these effects will be removed by the use of a highly enriched ^{28}Si sample. Furthermore we expect to observe an energy shift depending on the isotopic mass of the dopant sulfur (^{32}S and ^{34}S) and the host isotope (^{28}Si or ^{30}Si).

The deep centre sulfur was chosen as a first in a series of experiments on deeper centres in silicon because of its high diffusivity and the extensive literature available on sulfur in natural silicon. This facilitates the sample production as compared to other chalcogens like selenium or tellurium. Much of what is learned with the help of sulfur can later be applied to experiments with these other chalcogen dopants and other deep centres in general.

To conduct the experiment a high resolution Fourier transform spectrometer was used in an infrared absorption spectroscopy configuration. The limited material availability posed a spectroscopic challenge. To improve the signal strength and quality, optimizations to illumination conditions and filter combinations had to be done.

In the following parts of this thesis some background information about the sulfur impurity in silicon and isotope effects will be given. This is followed by a description of the sample preparation process and the experimental configuration. The spectroscopic results are then laid out in the last chapter.

Chapter 2

Theoretical Framework

2.1 The Sulfur Donor in Silicon

The chalcogen sulfur gives rise to a number of different donor centres in silicon [12]. These centres can involve one, two or more sulfur atoms and can be either neutral or ionized. In this work we investigated the centres S^0, S^+ and S_2^0. Here the superscript of the label denotes the ionization state of the donor, while the subscript indicates the number of atoms comprising the impurity centre with '2' standing for a sulfur pair. More complex structures carry the subscript 'c', but they are not relevant for this work. The S^0 and S^+ impurity centres are substitutional and occupy a tetrahedral site in the silicon host lattice as shown in Figure 2.1. The binding energy of the sulfur impurity centres is relatively large. Figure 2.2 shows that the binding energy of the S^+ centre lies roughly in the middle of the silicon band gap. Other centres like S_2^+, S^0 and S_2^0 have a smaller binding energy but are still considerably deeper than the shallow donor phosphorus.

These defect centres in the silicon crystal are helium-like, with sulfur having the atomic number 16, while silicon has 14. Hence sulfur has two more protons and two more valence electrons than the surrounding silicon atoms in the crystal. This gives rise to two different spectral series due to the different ionization states. These include the S^0 series, where one electron remains in the ground state while the second one can be involved in a transition, and also the singly ionized S^+ series, where the one

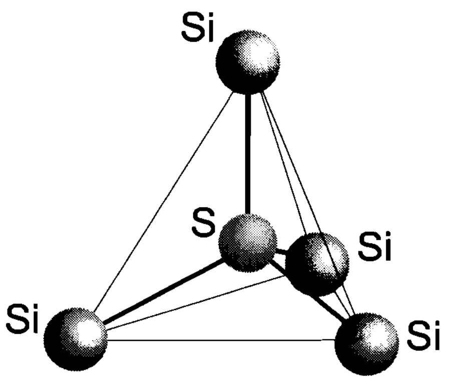

Figure 2.1: Tetragonal crystal structure of silicon with a substitutional impurity. The sulfur atom in the centre is surrounded by four nearest neighbour silicon atoms.

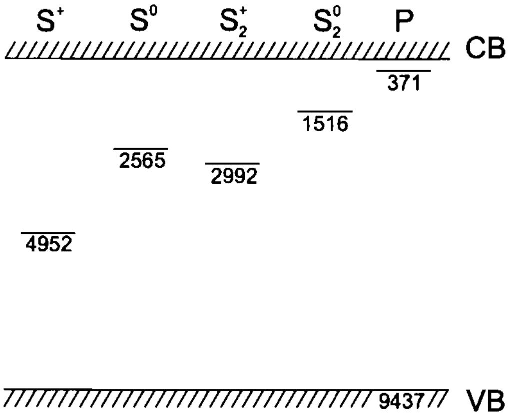

Figure 2.2: Ground state binding energies (in cm^{-1}) of different S and P impurity centres in Si and their location relative to valence band (VB) and conduction band (CB). [10]

remaining electron is involved in a transition. Despite this difference they both have typical 'hydrogenic' spectra [10], and thus the excited state binding energies for the sulfur donors can be calculated by means of the effective-mass theory (EMT). This has been done by Faulkner in 1969 [15] and earlier by Kohn and Luttinger in 1955 [16] and Kittel and Mitchell in 1954 [17]. It has been shown [12] that these calculations are in good agreement with experimentally determined values for p-like states of neutral donor centres. As required for the effective-mass approximation to be valid, these p-states have their orbitals in regions away from the donor centre-potential, where the potential varies only slowly over a unit cell.

Essentially the p-state spectra have features identical to the ones observed for shallow group V donors in silicon, such as the prototypical phosphorus impurity [9]. In fact, a simple scaling and shifting operation can transform the sulfur transition energies into the respective phosphorus transition energies.

In contrast to the p-states, the s-states, in particular $1s$, show a different behaviour. Silicon has six equivalent conduction band minima along the [100] directions. The central part of the potential for s-states causes a considerable interaction between the six valley states that are degenerate in EMT. Thus they are split into components of

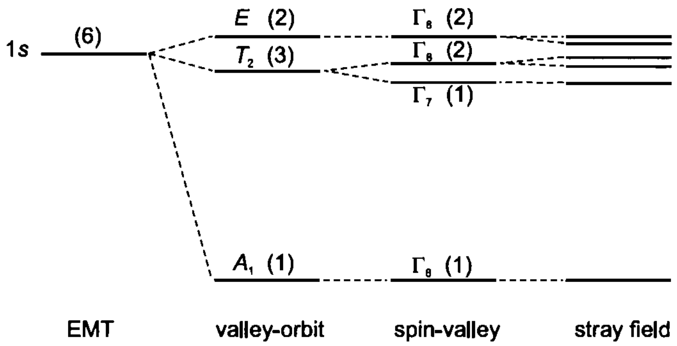

Figure 2.3: Multivalley splitting of $1s$ donor states in silicon. Degeneracies are given (without spin). [13]

lower degeneracy in accordance with the local symmetry of the donor centre [12].

For donor atoms sitting on tetrahedral lattice sites the central cell potential splits the sixfold degenerate s-state into a singlet (A_1), a triplet (T_2) and a doublet (E) (see Figure 2.3). Due to the localization of the central cell potential, this so called valley-orbit splitting is strongest for the $1s$-state, weak for higher s-states and negligible for other higher states like p, d [13].

Including spin in these considerations leads to a further splitting, the spin-valley splitting. The symmetry representations A_1 and E change to Γ_6 and Γ_8 respectively but the T_2 level makes the transition $T_2 \rightarrow \Gamma_7 + \Gamma_8$ and is therefore split. The p-character of the T_2 level makes interaction with the spin possible, with Γ_8 corresponding to a "pseudo" $p_{3/2}$ and Γ_7 to a "pseudo" $p_{1/2}$ state [13, 18]. The Γ_8 state is doubly degenerate and thus shifted by less than the nondegenerate Γ_7 level from the unsplit T_2 energy level with a ratio of $\frac{2}{1}$. The degeneracy of the Γ_8 level can be lifted by stress or electric fields [13]. A summary of the different splittings is given in Figure 2.3.

Both transitions, $1s(A_1) \rightarrow 1s(T_2)$ and $1s(A_1) \rightarrow 1s(E)$ are EMT forbidden since they are transitions between $1s$ states, while the T_2 transition is symmetry allowed. The E transition is symmetry forbidden. To be an allowed transition, one of the two states (ground or excited state) has to mix with another state. This could be a p-state or states from higher lying bands. The magnitude of the mixing depends on

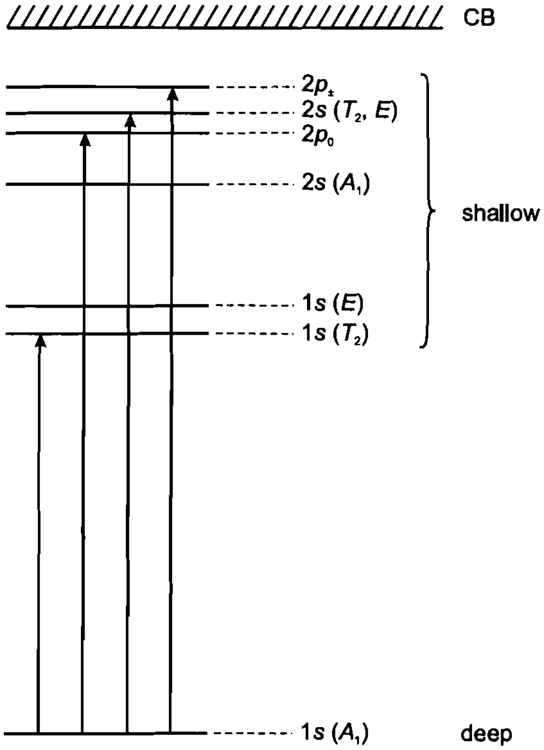

Figure 2.4: Energy spectrum of a deep substitutional donor in silicon. Symmetry allowed transitions are marked with arrows. [12]

the binding energy of the donor. For shallow donors no transitions between 1*s* levels have been observed in silicon. Deeper centres like chalcogens (sulfur), in contrast, show those EMT forbidden 1*s* transitions with an intensity comparable to the ground state to *p*-state transitions. Figure 2.4 gives an overview of the allowed transitions of a substitutional donor like sulfur in silicon.

The *p*-states of S^+ and S^0 resemble each other very much with one major difference. Due to the fact that in S^0 the excited electron effectively moves in the field of a hydrogen core with the second electron shielding the other core charge, whereas it is in the field of a doubly charged core in S^+, the energy spacing between the S^+ transitions is four times as large as between S^0 transitions. The transition energy in the hydrogen/Bohr model is proportional to the square of the core charge:

$$E_n = \frac{-m_e q_e^2 q_c^2}{8h^2\epsilon_0^2 n^2} \sim q_c^2 \tag{2.1}$$

2.2 Isotope Broadening

Previous research done on the shallow impurities phosphorus and boron in isotopically enriched silicon made it clear that the dominant broadening mechanism for many impurity absorption lines in ^{nat}Si is not the lifetime broadening as had been thought. The inhomogeneous broadening, rather, is a result of the isotopic randomness present in natural silicon [3, 6–8]. It has been shown that isotopically enriched silicon is the key to achieving narrower transition linewidths than before.

The inhomogeneous broadening of impurity absorption transitions due to the isotopic randomness of the silicon host material was explained in [7]. The broadening seen in ^{nat}Si or any sample of mixed isotopic composition is dominated by an effect which is independent of the small shifts in binding energy between pure ^{28}Si, ^{29}Si and ^{30}Si. The ground state wave functions of the impurities are fairly compact, and sample a relatively small volume surrounding the impurity ion. Hence in natural Si these wave functions are subject to relatively large fluctuations of the actual isotopic composition within this effective volume. These fluctuations in turn induce shifts of the ground state energies, which can be related to the known shifts of the conduction band energies with average isotopic composition. The excited state wave functions, on the other hand, are much more extended, and therefore sample isotopic compositions much closer to the average composition than the ground state wave function does. The difference in the isotopic composition sampled by the ground state and the excited state leads to an inhomogeneous broadening which is expected to become larger for deeper, and thus more compact, ground states. This inhomogeneous broadening leads to a Gaussian line shape.

After removing this inhomogeneous broadening by using isotopically enriched host material, in our case ^{28}Si, one is then often left with homogeneous broadening due to the lifetime of the excited state, indicated by a Lorentzian line shape. The lower limit to the observed linewidth is dictated by the uncertainty principle $\Delta E \cdot \tau = \hbar/2$. Thus the line width is given by the lifetime of the excited state. The longer the lifetime τ is, the smaller is ΔE and the FWHM.

2.3 Isotope Shifts

Isotope effects give rise to two different kinds of energy shifts. One is the result of the isotopic composition of the host material while the isotopic mass of the dopant can introduce an energy shift of the transition line as well.

2.3.1 Host Shift

Electronic Shift

It has been observed for boron impurities in diamond composed of ^{12}C and enriched ^{13}C that the host isotopic mass introduces a shift of the transition energies [19]. This has been explained as a result of the dependence of the binding energy E_B on the effective mass m^* and the static dielectric constant ϵ_0 [20]. In the case of diamond the contribution of ϵ_0 to the energy shift was found to be negligible, but for the silicon host it has to be included in the model, as it has been shown for the shallow donor phosphorus and acceptor boron [8]. The dependence of ϵ_0 and m^* on the isotopic mass scales the ground state and excited state binding energies by an identical factor, which means the shift in transition energy increases with the energy of the transition or with decreasing final state binding energy. Thus the largest shifts are observed for transitions to the highest excited states.

To estimate this energy shift the equation for the ionization energy of shallow (hydrogenic) levels in semiconductors $E_B = Ry \cdot m^*/\epsilon_0^2$ can be used, where Ry is the hydrogen Rydberg. Donor and acceptor binding energies are scaled identically by the influence of the average isotopic mass M on ϵ_0. Reference [8] shows how the difference in the dielectric constant ϵ_0 between ^{28}Si and ^{30}Si can be estimated from the zero-point temperature renormalization of ϵ_0 by the electron-phonon interaction, which is proportional to $M^{-1/2}$. The reference also explains how to obtain the influence of the zero-point renormalization on the effective mass m^* of donors.

We expect to observe a similar behaviour of the transition energy as previously observed for shallow impurities in isotopically enriched silicon for the deep centre sulfur.

Local Vibrational Modes

Following Pajot et al. [11], a model for an isotope shift due to mass dependent local vibrational modes (LVM) can be developed. The term local vibrational mode often refers to lighter atoms in the crystal with phonon energies above the highest lattice phonon energy. Here it refers to the fact that every atom is vibrating and contributing to the vibrational energy of the crystal. Considering the tetrahedral SSi_4 cluster in the valence force approximation and the simplification that the radial force constant is considerably larger than the transverse force constant, only two vibrational modes are present. Mode α_1 is fully symmetric and transforms according to the Γ_1 irreducible representation of the T_d point group. The second one, a triply degenerate asymmetric mode τ_2, transforms according to Γ_5. Besides the purely electronic contribution to the energy E, we are then left with the zero-point energies in the electronic ground and excited states. The contribution E_{vib} of the two vibrational modes α_1 and τ_2 to E is then:

$$E_{\text{vib}} = \frac{\hbar}{2}[(\omega_1^e - \omega_1^g) + 3(\omega_5^e - \omega_5^g)]. \tag{2.2}$$

Here ω_1 and ω_5 are the mode frequencies of the irreducible representations Γ_1 and Γ_5 respectively. The superscript refers to the ground and excited states and the factor of 3 originates from the degeneracy of the τ_2 mode. This describes the case of four equal silicon atoms in the cluster. When one of them is replaced with a different isotope ^{x}Si, the point group symmetry of this new $SSi_3{}^xSi$ cluster changes to $C_{3\nu}$. As a consequence the τ_2 mode with its frequency ω_5 splits. The resulting modes transform according to the Γ_1 (singly degenerate) and Γ_3 (doubly degenerate) representations of the $C_{3\nu}$ group, with frequencies of ω_{51} and ω_{53} respectively. The frequency ω_1 of the α_1 mode shifts to ω_{11}. Thus we obtain a new zero-point energy contribution E_{vib}^x

to the energy E_x of the optical transition:

$$E^x_{\text{vib}} = \frac{\hbar}{2}[(\omega^e_{11} - \omega^g_{11}) + (\omega^e_{51} - \omega^g_{51}) + 2(\omega^e_{53} - \omega^g_{53})]. \tag{2.3}$$

Hence the isotope shift due to the replacement of one ^{28}Si atom in the SSi$_4$ cluster is the difference $\Delta E_{\text{iso}} = E^x_{\text{vib}} - E_{\text{vib}}$ between expressions (2.3) and (2.2). To observe this isotope shift, the mode frequencies in the electronic ground and excited states have to be different. Those differences in mode frequencies are a result of the difference in electron density at the impurity site. In the ground state the excess electron is much more localized, and its presence corresponds to a filling of the antibonding orbitals of the bonds in the cluster. The result is a softening of the force constants and a lower mode frequency. In the excited state the electron density is much lower and thus the bond softening is weaker. Thus we expect to see multiple absorption lines due to the different local vibrational modes of the differently composed SSi$_4$ clusters. The isotope shift is then:

$$\begin{aligned}\Delta E_{\text{iso}} &= \frac{\hbar}{2}[(\omega^e_{11} - \omega^e_{1}) - (\omega^g_{11} - \omega^g_{1}) + (\omega^e_{51} - \omega^e_{5}) - (\omega^g_{51} - \omega^g_{5})] &(2.4)\\ &= \frac{-\hbar\omega^e_1}{4}\kappa\left[1 + \frac{3}{\sqrt{1+\Lambda}}\right]\left(1 - \sqrt{\frac{k_g}{k_e}}\right), &(2.5)\end{aligned}$$

where the following substitutions were used: $\omega_{11} = \omega_1\sqrt{1-\kappa}$, $\omega_5 = \omega_{53} = \omega_1\sqrt{1+\Lambda}$, $\omega_{51} = \omega_1\sqrt{1+\Lambda-3\kappa}$. Here $\omega_1 = \sqrt{k/m}$, $\kappa = \Delta m/4(m+\Delta m)$ with $\kappa \ll 1$ and $\Lambda = 4m/3M$ where m is the mass of a ^{28}Si atom, Δm is the mass difference between ^{28}Si and ^{x}Si and M is the mass of the sulfur atom. With the spring constant of the ground state k_g being smaller (softer bond) than k_e, ΔE_{Si} is negative. This means that the expected satellite peaks involving the heavier isotopes ^{29}Si and ^{30}Si occur on the low energy side of the main ^{28}Si peak.

2.3.2 Dopant Shift

Isotope shifts for impurities in semiconductors have been shown and explained before in [21, 22] and more specific to our experiment in [7, 8] for the shallow impurity boron in isotopically enriched ^{28}Si. In the case of boron, the heavier isotope ^{11}B has a lower binding energy than the lighter ^{10}B. When observed with high enough resolution, this results in a ^{11}B/^{10}B doublet with a constant separation of $0.15\,\mathrm{cm}^{-1}$ for every absorption line throughout the p-state spectrum.

The two different B isotopes have slightly different ground state binding energies. This is a result of a different zero point energy of the local vibrational modes of the impurity isotopes. When the impurity is ionized or excited, i.e. the electron is not localized any more, these zero point energies change. The charge distribution of ground and excited states is not dependent on the impurity mass and thus the spring constants change by the same amount for each isotope. But the vibrational energy also depends on the impurity mass, resulting in a different shift for each isotope. The difference between those LVM-energy shifts is what causes the energy shift between different impurity isotope absorption lines. The scaling factor is in almost all cases essentially the same for any excitation level or ionization and thus the shift remains the same throughout one spectrum.

A similar behaviour has been observed before for sulfur centres in silicon [11] and thus we expect to see this effect as well for the different sulfur isotopes in our experiment, mainly ^{32}S and ^{34}S. Indeed this is true for the p-states and S^0 $1s(T_2)$, where the ^{34}S absorption line is observed at lower energy than the ^{32}S transitions. In strong contrast to this, the S$^+$ $1s(T_2)$ absorption line exhibits an opposite behaviour with the ^{34}S transition having a higher binding energy. This effect was explained by Pajot et al. in [11].

Chapter 3

Experimental Methods

This chapter presents the details about the samples and the experimental setup. The first section discusses the materials used to prepare the samples and explains the process of sample preparation. This is then followed by an overview of Fourier transform spectroscopy and ends with a description of the experimental setup and technical means utilized to carry out the experiments.

3.1 Samples

3.1.1 Materials

Several samples were prepared to study the isotope dependence of the transition energies and to observe how the isotopic randomness influences the width of the absorption lines. Therefore a variety of different host and dopant material compositions were used. As a host material, specimens with different silicon isotope enrichment were used. In addition, for natural silicon, samples with different doping levels (ultra high purity (UHP) Si and Si:B) were available to optimize different aspects of the experiment. This was not feasible with the enriched materials because of their limited availability.

As far as the natural silicon is concerned, UHP n-type Si was obtained from Topsil Semiconductor Materials and Si:B (45 Ω-cm) produced by Virginia Semiconductor was

Table 3.1: Isotopic composition and impurity concentrations (in cm^{-3}) of the silicon samples used for sulfur diffusion. From [23] for ^{28}Si and [26] for ^{30}Si.

	^{28}Si	^{29}Si	^{30}Si	[P]	[B]
^{28}Si	99.991 %	0.0075 %	0.0015 %	2×10^{12}	5×10^{13}
^{30}Si	2.50 %	7.70 %	89.80 %	2.4×10^{13}	–
^{nat}Si:B	92.2 %	4.7 %	3.1 %	–	3×10^{14}
^{nat}Si (UHP)	92.2 %	4.7 %	3.1 %	1.3×10^{12}	3.3×10^{12}

used for *p*-type samples.

The ^{28}Si material used for this study was obtained from the Avogadro Project [23], an effort to redefine the kilogram in terms of the Avogadro constant. This material had previously proven to be of excellent quality [24, 25], both in terms of isotopic enrichment as well as chemical purity. It has to be noted that the chemical purity of isotopically enriched silicon at the present stage does not yet meet that of UHP natural silicon. The ^{28}Si sample is *p*-type and is a fraction of a larger piece labelled Si28-9.1Pr11.7. The material is only available in limited amounts and thus we had to use very small and thin pieces, making it more difficult to achieve a reasonable signal to noise ratio.

The ^{30}Si sample has an isotopic enrichment of 89.80 % ^{30}Si. Due to the lower natural abundance it is more difficult to achieve higher enrichment levels for ^{30}Si and at the same time keep the level of chemical impurities low. Therefore this material does not match the enrichment of the ^{28}Si sample and yet is one of the best ones available at the time. The sample was provided by Eugene E. Haller, UC Berkeley, California. The material is related to the project described in [26].

A summary of isotopic enrichment and impurity concentrations of the different silicon samples used for the experiment is given in Table 3.1.

On the sulfur dopant side, two different compositions were used. Natural sulfur was obtained from Puratronic with a chemical purity of 99.9995 % and isotopic abundances of 94.93 % ^{32}S, 0.76 % ^{33}S, 4.29 % ^{34}S and 0.02 % ^{36}S. The enriched ^{34}S was obtained from ICON Isotopes and has a specified isotopic enrichment of 90 % ^{34}S. Spectra give evidence that the actual enrichment is considerably higher than the nominal value (see Table 4.6). Sulfur has a high diffusivity of $D = 11.6 \times 10^{-13}\,\mathrm{m^2/s}$ at 1100 °C, following the Arrhenius law in a temperature region that is accessible with our furnace (1328–1671 K) [27], allowing a relatively quick sample preparation.

3.1.2 Sample preparation

In order to obtain a clear image of the different isotope effects, different host and impurity isotopic compositions were used to produce five categories of samples:

$$^{28}\mathrm{Si}{:}^{\mathrm{nat}}\mathrm{S},\ ^{28}\mathrm{Si}{:}^{34}\mathrm{S}$$

$$^{30}\mathrm{Si}{:}^{\mathrm{nat}}\mathrm{S}$$

$$^{\mathrm{nat}}\mathrm{Si}{:}^{\mathrm{nat}}\mathrm{S},\ ^{\mathrm{nat}}\mathrm{Si}{:}^{34}\mathrm{S}$$

The samples were all prepared in a similar way as described in the literature [12, 14]. The silicon sample together with a small piece of the dopant sulfur (approximately 5 mg), was inserted into a quartz tube that was closed at one end. The tube was then evacuated and at the same time carefully necked down with a torch flame and finally closed to form a sealed ampule. Care was taken to avoid overheating and decomposition of the dopant. To avoid cross contamination the differently composed hosts (and dopants) had to be diffused separately.

These ampules were then inserted into a preheated furnace. After the heat treatment they were removed from the hot furnace and quenched rapidly in methanol. The ampule as well as the samples themselves survived the quench process without breaking. The samples were taken out of their ampules and were reheated to 1100 °C for several minutes before requenching them in methanol. This is necessary to reduce the sulfur pair formation to a minimum and to keep the sulfur at substitutional lattice sites rather than interstitial sites [28], since the interest in this study mainly lies in isolated sulfur rather than in S_2 pairs.

The approximate concentration of sulfur in the silicon sample can be calculated. Assuming that the surface concentration is at its solid solubility limit of $c^{\mathrm{eq}} = 3 \times 10^{15}\,\mathrm{cm^{-3}}$ [29, chap. 4.2 Silicon] at 1100°C together with the mentioned diffusivity of

$D = 11.6 \times 10^{-13}\,\mathrm{m^2/s}$ at 1100 °C, the impurity concentration $N(x,t)$ is given by [30]:

$$N(x,t) = c^{\mathrm{eq}} * \operatorname{erfc} \frac{x}{2\sqrt{Dt}}. \tag{3.1}$$

Our samples have a thickness of approximately 1 mm. Diffusion takes place on both sides of the sample, hence we can calculate the concentration at $x = 0.5\,\mathrm{mm}$ to obtain a lower boundary. With $t = 20\,\mathrm{h}$ the error function evaluates to 0.22 so that we obtain $N(0.5\,\mathrm{mm}, 20\,\mathrm{h}) \approx 6.6 \times 10^{14}\,\mathrm{cm^{-3}}$. Effectively the concentration at the centre of a 1 mm thick sample is twice as high. However, we did not verify the sulfur concentration experimentally.

During their time in the furnace all samples eroded. Vapour transport within the ampule to cooler portions occurred and polycrystalline silicon was deposited at the cooler end of the ampule. The samples were mechanically polished to remove the erosion features and etched in a hydrofluoric acid/nitric acid solution ($HF + HNO_3$) to remove surface damage. After this process is carried out carefully and thoroughly the samples are usually strain free. Any residual strain would degrade the quality of the spectra.

The $^{\mathrm{nat}}$Si:$^{\mathrm{nat}}$S sample was prepared using a UHP Si substrate. It was kept in the furnace for 2 hours at 1000 °C and another 20 hours at 900 °C. It was found that the concentration of isolated sulfur centres was not high enough and subsequently the sample was then quenched into methanol after being reheated to 1100 °C for a duration of 7 minutes. After this treatment the concentration of S_2 centres was reduced significantly and the majority of the detected sulfur centres were isolated S. This made the importance of rapid quenching obvious and thus it was applied to all subsequently produced samples.

In addition to this an older UHP Si:S sample was used. The spectrum of this sample was comparable to that of the newly prepared one and no sign of decay or deterioration due to its age (~10 years) was visible.

The $^{\mathrm{nat}}$Si:^{34}S Samples were made using Si:B and UHP Si for diffusion. The UHP Si sample was used to observe transitions of neutral centres like S^0 and S_2^0 while the Si:B sample is better suited to observe ionized S^+ impurity centres due to the higher B acceptor concentration. The ampule was kept in the furnace for about 24 hours at 1100 °C.

The ^{28}Si:$^{\mathrm{nat}}$S and ^{28}Si:^{34}S samples were each enclosed in a smaller ampule with an inner diameter of only 7 mm together with $^{\mathrm{nat}}$S or ^{34}S for diffusion. Both were then kept in the furnace for 20 hours at 1100 °C. In contrast to the normal procedure, the ampule with ^{34}S was backfilled with argon (Ar) at a pressure of 250 mmHg. This technique has proven to successfully reduce vapour transport and thus it reduces the amount of erosion and potential causes of strain fields. Note that a complete dataset for the ^{28}Si:^{34}S sample is not available since it was produced at a later time, mainly to improve on the S$^+$ $1s(T_2)$ spectrum. The sample is not expected to deliver fundamentally improved results for other spectral regions, as compared to ^{28}Si:$^{\mathrm{nat}}$S.

The ^{30}Si:$^{\mathrm{nat}}$S sample was kept in the furnace for 24 hours at 1100 °C.

3.2 Fourier transform spectroscopy

Typically, and in our case, a Fourier transform spectrometer is a Michelson interferometer, originally designed in 1891 [31]. The Michelson interferometer splits the incoming beam into two and then recombines those again after a path difference has been introduced to one of them by means of a scanning mirror (see Figure 3.1). The output signal can then be recorded as a variable of the path difference δ, also called retardation.

Given this geometry, a monochromatic light source would interfere with itself at the detector due to the path difference of the two beams resulting in the following intensity $I'(\delta)$ [32]:

$$I'(\delta) = 0.5I(\nu)(1 + \cos 2\pi\nu\delta), \tag{3.2}$$

where $\nu = 1/\lambda$ is the wavenumber and $I(\nu)$ is the source intensity. The constant component does not contain any relevant information. The modulated part is referred to as the interferogram $I(\delta)$. In a real world spectrometer other factors like the beam splitter, the detector and the amplifier modify the signal. Those can be modelled with

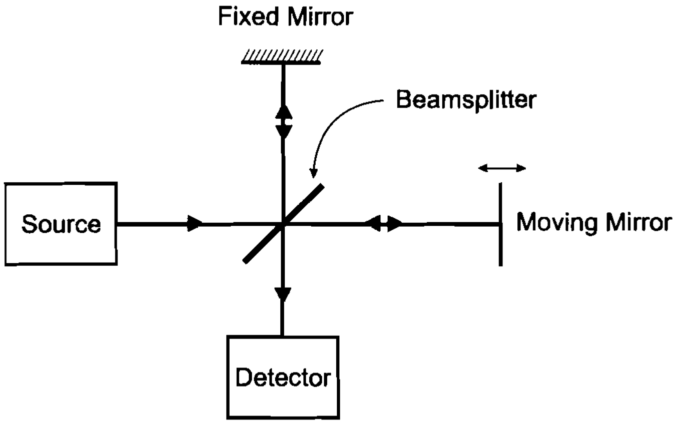

Figure 3.1: Schematic of a Michelson interferometer

a single wavenumber dependent factor $H(\nu)$. Setting $B(\nu) = 0.5H(\nu)I(\nu)$ gives for the interferogram:

$$I(\delta) = B(\nu)\cos 2\pi\nu\delta. \tag{3.3}$$

$I(\delta)$ is the cosine Fourier transform (FT) of $B(\nu)$. To obtain the spectrum $B(\nu)$ the FT of the interferogram $I(\delta)$ has to be calculated.

When taking (3.3) from a monochromatic to a continuous source, the interferogram is given by an integral over the wavenumber:

$$I(\delta) = \int_{-\infty}^{+\infty} B(\nu)\cos 2\pi\nu\delta \cdot d\nu, \tag{3.4}$$

with its cosine Fourier transform being

$$B(\nu) = \int_{-\infty}^{+\infty} I(\delta)\cos 2\pi\nu\delta \cdot d\delta. \tag{3.5}$$

Here we see that it is possible to obtain a scan of the entire spectrum over all wavenumbers but on the other hand equation (3.5) also shows a limitation of the Fourier transform spectrometer. A real interferometer will always have a limited retardation δ and as we shall see this results in a finite resolution.

The maximum retardation of the interferogram is restricted to a finite length Δ.

A simple truncation function $D(\delta)$, also called the boxcar function, would be

$$D(\delta) = \begin{cases} 1 & \text{if } -\Delta \leq \delta \leq +\Delta \\ 0 & \text{if } \delta > |\Delta| \end{cases} . \tag{3.6}$$

The spectrum is then modified so that

$$B(\nu) = \int_{-\infty}^{+\infty} I(\delta) D(\delta) \cos 2\pi\nu\delta \cdot d\delta. \tag{3.7}$$

Hence the spectrum is a convolution of the FT of $I(\delta)$ and $D(\delta)$. While the FT of $I(\delta)$ results in the true spectrum, the FT of $D(\delta)$ is

$$f(\nu) = 2\Delta \cdot \operatorname{sinc} 2\pi\nu\Delta, \tag{3.8}$$

a sinc-function as shown in Figure 3.2.

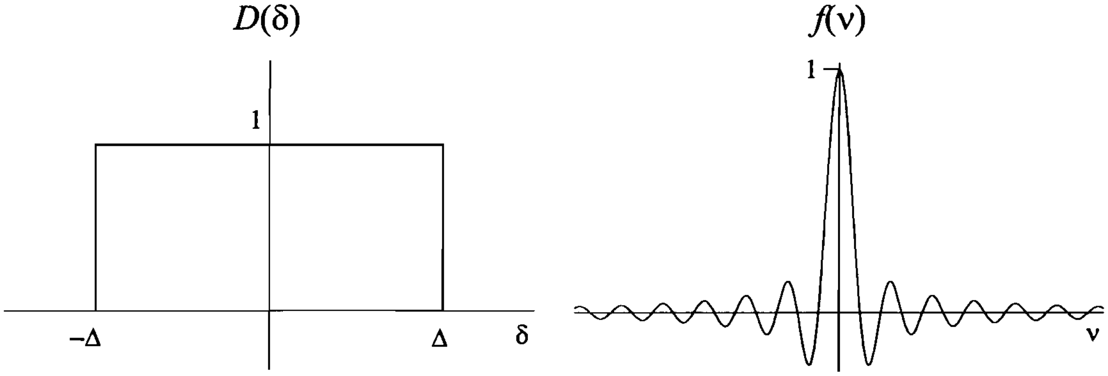

Figure 3.2: Plot of the $D(\delta)$ boxcar function and its Fourier transform $f(\nu) \sim \operatorname{sinc} \nu$.

When the true line of infinitessimal width is convoluted with a sinc function it obtains a finite width. For a boxcar truncation function it is found that the full width at half maximum (FWHM) imposed by the finite path length is [33]:

$$\text{FWHM} = \frac{1.207}{2\Delta}. \tag{3.9}$$

The maximum retardation in the Bomem DA8 spectrometer used for this study is $\Delta = 250\,\text{cm}$, corresponding to a maximum resolution of $0.0024\,\text{cm}^{-1}$ using the boxcar truncation.

Due to its shape the sinc function introduces "ringing" in the spectrum surrounding sharp features that are narrower than the used resolution. Using different truncation functions like Blackman-Harris (in a process called apodization) these can be reduced at the cost of increased FWHM [32]. The high resolution spectra in this work are recorded with $\Delta = 200\,\mathrm{cm}$ and a boxcar truncation, corresponding to a resolution of $0.003\,\mathrm{cm}^{-1}$. For all other spectra a Blackman-Harris apodization was used.

3.3 Experimental Setup

3.3.1 Fourier transform spectrometer

In this study a Bomem DA8 Fourier transform spectrometer was used. It is equipped with a scanning tube capable of a 250 cm retardation of which 200 cm were used for the high resolution spectra. The resolution was verified to be better than $0.007\,\mathrm{cm}^{-1}$ with the help of gas lines. Its internal light sources, a globar and a quartz lamp, were used for our experiments together with appropriate beam splitters (KBr and CaF_2 respectively). The cryostat's tail was placed inside the evacuated spectrometer and HgCdTe, InSb or InAs detectors (all liquid nitrogen cooled) were used according to the desired energy range. Figure 3.3 shows a schematic diagram of the spectrometer and its peripherals.

3.3.2 Cryostat

For this study a continuous flow, variable temperature cryostat was used. This choice was made mainly due to the windows of this cryostat that are suitable for our experiment and the size restrictions given by the spectrometer. It has ZnSe windows on the cold side and wedged BaF_2 windows on the outside. The wedge shape eliminates interference fringes that are otherwise caused by parallel window surfaces. Almost all experiments were carried out using this cryostat as an immersion dewar at superfluid helium temperatures. This was done by filling the sample chamber with liquid helium from the reservoir through a needle valve. After closing the needle valve, pressures as low as 2 mm Hg in the sample chamber can be achieved with a mechanical vacuum

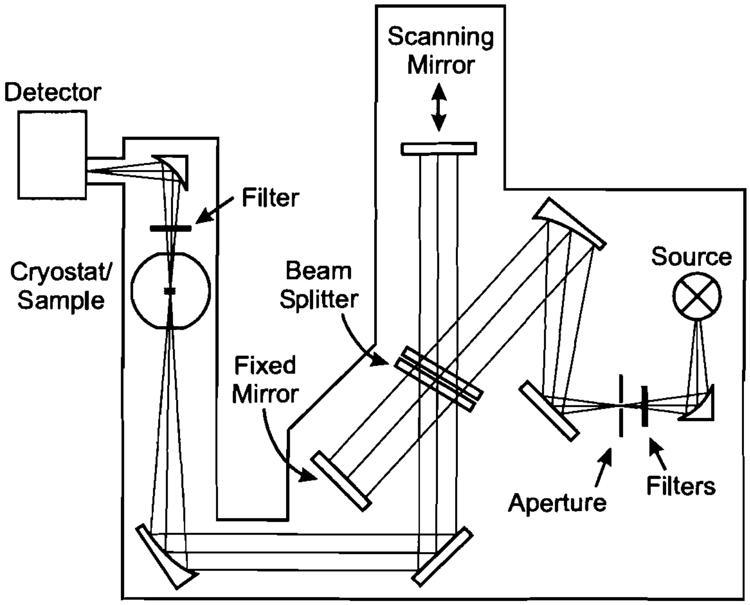

Figure 3.3: Experimental setup with Fourier-transform interferometer, Cryostat and Detector. The light from the source is focused into a circular aperture and then reflected onto the beamsplitter as a collimated beam. After passing through the actual interferometer part with its two arms the light is focused onto the sample in the cryostat. With another mirror it is finally focused onto the detector.

pump. Reducing the He vapour pressure this way allows one to work in superfluid helium at a temperature of $\sim 1.5\,\mathrm{K}$. In this study the main advantage of working with superfluid helium is an improved signal to noise level as compared to helium at $4.2\,\mathrm{K}$. In the superfluid state, helium boil-off bubbles disappear and do not interfere with the light beam any more. In addition, thermally activated excitations in the sample are reduced to a minimum.

The samples were mounted on a brass sample holder. They were loosely held in place, with their own weight being the only force on them, to avoid any mechanical strain. Special care was taken to eliminate light leaks around the samples since those could potentially lead to a saturation of the detector or shift the background, making it difficult to calculate the absorbance.

The dewar was positioned in the spectrometer so that the samples were at the focal point of the light beam.

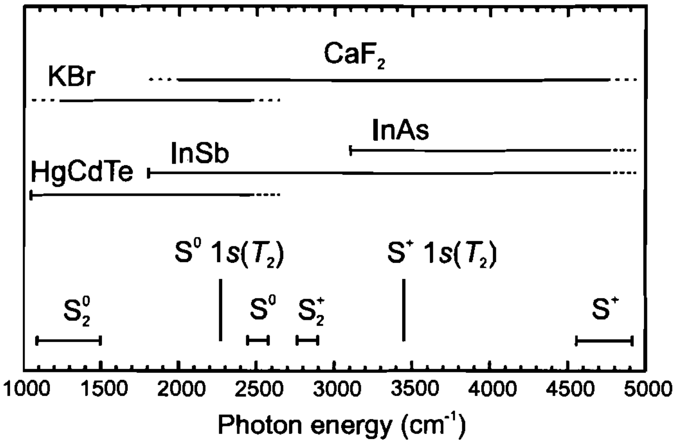

Figure 3.4: Spectral region of beamsplitters, detectors and transitions (top to bottom).

3.3.3 Detectors, Filters and Illumination Conditions

Several combinations of detectors and filters were used to record spectra in different energy regions (Figure 3.4) and to optimize the signal to noise ratio, especially for the S^+ $1s(T_2)$ transition. All detectors are liquid nitrogen cooled.

To observe S^+ (and S_2^+) absorption lines, in general a quartz source together with a 1038 nm long pass filter (LP) was used with no extra white light to reduce the amount of above-band gap light illuminating the sample. This way the neutralization of the sulfur centres was avoided, ensuring a high number of S^+ centres. The S^+ $1s(T_2)$ absorption line required special attention due to its weakness and several attempts have been made to improve the signal to noise ratio. It was found that the Quartz-Halogen source together with the 1038 nm LP filter provide good illumination conditions, and a 130 nm wide band pass filter centered on 2850 nm (3509 cm^{-1}) between sample and detector suppresses much of the black body radiation and thus reduces the noise level of the InAs detector, which has a cut-on energy of $\sim$ 3100 cm^{-1}. The S^+ $1s(T_2)$ transition ($\sim$ 3462 cm^{-1}) lies close to the centre of the band pass filter.

For S^0 transitions an InSb detector (cut on-energy $\sim$ 1800 cm^{-1}) was used with the Quartz-Halogen lamp and some extra white light illumination. The white light contributes to the neutralization of the impurity centres and thus to a high number of neutral S^0 centres and narrower linewidths due to the reduction of the random electric fields resulting from ionized impurities. No filters were used for these experiments.

To obtain spectra of S_2^0 transitions, a HgCdTe detector (with a cut on energy of less than $1000\,\mathrm{cm}^{-1}$) together with a Globar source and extra white light was used, as these transitions are at lower energy.

A CaF_2 beam splitter was used in combination with InAs and InSb detectors while the experiments involving the HgCdTe detector were conducted with a KBr beam splitter.

Chapter 4

Experimental Results and Discussion

This chapter presents the results obtained from the experiment conducted [34], along with relevant discussions. The main interest in this work lies on the S^+ $1s(T_2)$ transition. Hence the group of S^+ transitions is discussed in detail first. This is followed by a discussion of the S^0 transitions and closed with a look at the S_2^0 absorption transitions.

Figure 4.1 summarizes the most interesting part of the spectrum. It shows an interesting comparison of the $1s(T_2)$ and p-states of S^+ and S^0. The energy axis of the S^+ spectrum is compressed by a factor of four and shifted so that the S^+ p-states line up with S^0 p-states. Thus the S^+ transitions have a separation four times larger than the S^0 transitions. As explained in Section 2.1, this is the result of the S^+ centre being more helium like as opposed to the hydrogen like S^0 centre.

4.1 The S^+ transitions

4.1.1 Isotope effects observed at the S^+ $1s(T_2)$ transition

The composition of our samples is chosen so that we can observe two different effects due to changes in isotopic mass. With the help of different samples, different

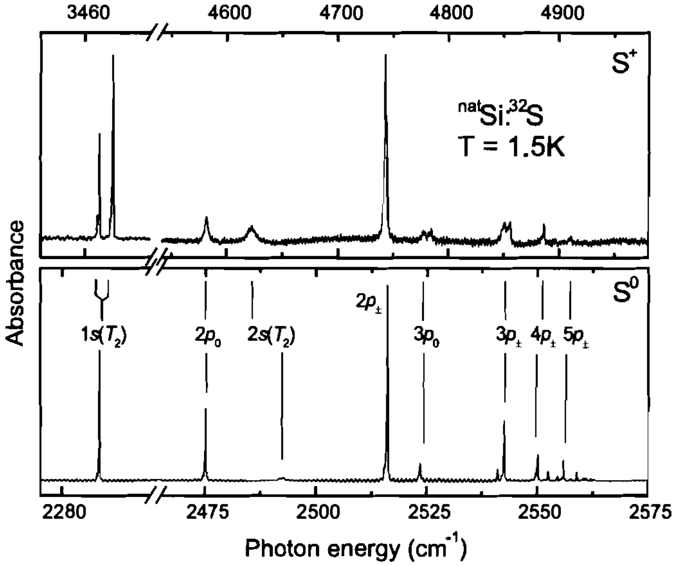

Figure 4.1: S^+ and S^0 ground state ($1s(A_1)$) to p-state transitions in ^{nat}Si stacked for better comparison. The upper scale for S^+ is four times larger than the lower one for S^0. Spectra were recorded at 1.5 K.

components and phenomena in the spectra can be identified easily. The S^+ $1s(T_2)$ absorption transition exhibits several different isotope effects. These are discussed below for the different samples studied in this work. In this section we will first discuss satellite peaks due to local vibrational modes in natural silicon, followed by isotope broadening shown with the example of ^{28}Si and finally we will take a look at host and impurity isotope shifts.

LVM satellite peaks

^{nat}Si:^{nat}S and ^{nat}Si:^{34}S The S^+ $1s(T_2)$ spectra of natural sulfur (^{nat}S or ^{32}S) is shown in Figure 4.2 and the one of enriched ^{34}S in natural silicon (^{nat}Si) in Figure 4.3.

The two absorption lines originate from the $1s(A_1) \rightarrow 1s(T_2)$ transition. The final state is split into a Γ_7 and a Γ_8 representation. In both spectra low energy satellites L_1, L_2 and L_3 can be seen (using the labelling scheme of [11]). These satellites are a silicon isotope effect. The basic principle of this energy shift in local vibrational modes was laid out in Section 2.3.1. In addition to this, Figure 4.2 also shows high frequency

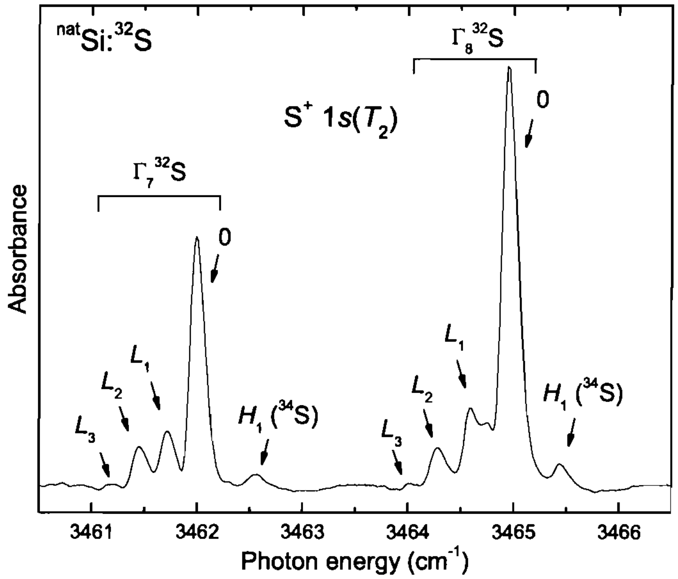

Figure 4.2: Fine structure of S^+ $1s(T_2)$ in $^{\mathrm{nat}}Si$ at a resolution of $0.100\,\mathrm{cm}^{-1}$ and a temperature of 1.5 K. Satellites labeled L_i are due to Si isotope effects, H_1 due to S isotope effects.

satellites H_1, originating from a sulfur isotope effect (explained in Section 2.3.2), to which we will come back at a later point. As we will see, the order of the satellites is basically reversed in our ^{30}Si sample and they are not present in ^{28}Si, confirming that they are a silicon isotope effect.

Considering that the substitutional impurity sulfur is surrounded by four nearest neighbour silicon atoms, the shifts in transition energy between the satellites L_1, L_2 and L_3 can be explained by the different isotopic composition of the SSi_4 cluster. The most probable surrounding of the sulfur impurity is of course four ^{28}Si atoms ($^{28}Si_4$, labelled '0'). Then it is possible to substitute one ^{28}Si atom with either ^{29}Si ($^{28}Si_3{}^{29}Si$, labelled L_1) or ^{30}Si ($^{28}Si_3{}^{30}Si$, labelled L_2). Another possibility is to substitute two ^{28}Si atoms. Possible combinations are $^{28}Si_2{}^{29}Si_2$ and $^{28}Si_2{}^{29}Si^{30}Si$. Judging from the figures and Table 4.2, the energy of the satellites scales linearly with the total mass difference of the Si_4 cluster. Thus the first of these two, with a total mass difference of 2 (with respect to $^{28}Si_4$) makes a small contribution to L_2 while the latter one is labelled L_3. Any other combinations have very low probabilities and thus are difficult to observe.

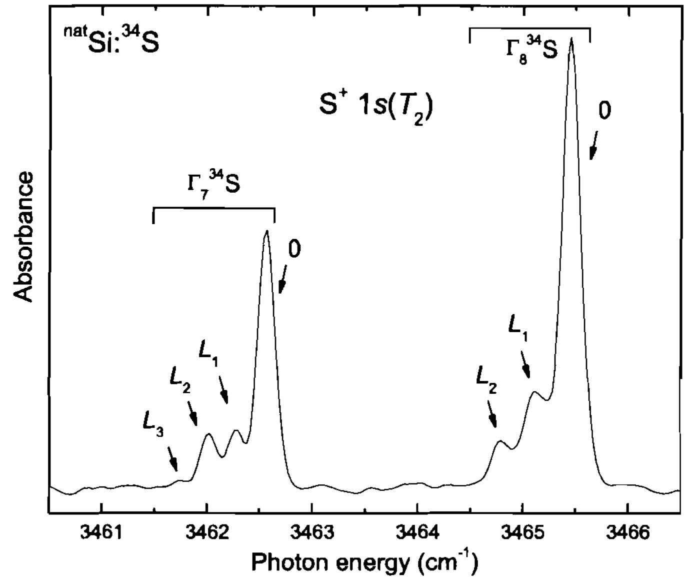

Figure 4.3: Fine structure of S^+ $1s(T_2)$ in ^{nat}Si diffused with ^{34}S at a resolution of $0.100\,cm^{-1}$ and a temperature of 1.5 K. Satellites labeled L_i are due to Si isotope effects. Note that H_1 is not present here.

Using the isotopic abundances of ^{nat}Si given in Table 3.1 the probabilities for the occurrence of these combinations can be calculated. The probabilities normalized to ^{28}Si are 0.20, (0.13 + 0.02) and 0.02 for L_1, L_2 and L_3, respectively. Comparing this to our data in Figures 4.2 and 4.3 we find for the ratio L_1/'0' $= 0.21 \pm 0.01$ and L_2/'0' $= 0.15 \pm 0.04$. L_3 is rather weak and not suitable for a representative comparison. Using the relative isotopic abundance of 5 % ^{34}S in ^{nat}S and comparing it to a measured value of $H_1/0 = 0.050 \pm 0.005$, H_1 can be identified as the $1s(T_2)$ transition of ^{34}S centres. Naturally, this H_1 satellite peak transforms into the main peak ('0') when enriched ^{34}S is used as shown in Figure 4.3. On the other hand, the absorption of the residual ^{32}S in this sample is hidden by the stronger L_i satellites. Note that for S^+ $1s(T_2)$ the binding energy of the heavier isotope ^{34}S is higher than that of the lighter isotope ^{32}S. This is in contrast to the usual isotope shift that was observed and described earlier in Section 2.3.2 and [7, 8] and will be discussed later.

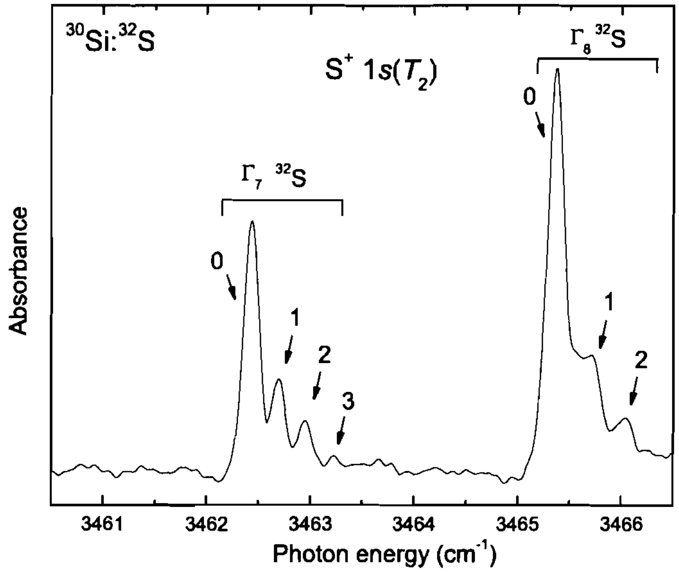

Figure 4.4: Fine structure of S^+ $1s(T_2)$ in ^{30}Si diffused with ^{nat}S at a resolution of 0.050 cm^{-1} and a temperature of 1.5 K. Satellites labeled '1', '2' and '3' are due to Si isotope effects. Satellite 3 of $1s(T_2)$ Γ_8 is too weak to be observed in this spectrum.

^{30}Si:^{nat}S Figure 4.4 shows the S^+ $1s(T_2)$ transition of ^{nat}S in our ^{30}Si sample. As shown in Table 3.1, the isotopic enrichment of our ^{30}Si sample is similar to that of natural silicon with the difference that here ^{30}Si is enriched to approximately 89.80 % and it contains roughly as much ^{29}Si and ^{28}Si as ^{nat}Si contains ^{29}Si and ^{30}Si. It is immediately visible that the order of the satellite peaks is reversed in ^{30}Si, thus leading us to conclude that they are indeed the result of a silicon isotope effect which is reversed here due to the opposite isotope distribution in the ^{30}Si sample as compared to ^{nat}Si. This reversal of masses changes the sign of the energy shift calculated in Section 2.3.1 and hence we see the satellites at the high energy side of the main peak. In this sample the majority of lattice sites is occupied by ^{30}Si atoms. With a small probability similar to that calculated before, some of the ^{30}Si atoms in the SSi_4 cluster at an impurity site can be replaced with a ^{29}Si or ^{28}Si atom. In Figure 4.4 transitions corresponding to those clusters have the labels '1' and '2' assigned respectively. The transition labelled '3' is a result of two ^{30}Si atoms being replaced by one each of the lighter species. As before, a $^{30}Si_2{}^{29}Si_2$ cluster is contributing to '2'. Using the isotopic

Table 4.1: Positions and FWHM of the components of S^+ $1s(T_2)$ Γ_7 and Γ_8 in ^{30}Si (in cm^{-1}). Shifts are given with respect to the line labelled '0'. Accuracy: ±0.020.

	^{30}Si:^{nat}S			
	0	1	2	3
S^+ $1s(T_2)$ Γ_7	3462.430	3462.696	3462.952	3463.208
FWHM	0.172	0.131	0.203	-
shift	0.000	+0.266	+0.522	+0.778
S^+ $1s(T_2)$ Γ_8	3465.37	3465.713	3466.007	-
FWHM	0.192	0.219	0.213	-
shift	0.000	+0.343	+0.637	-

enrichment given in Table 3.1 we find that all other combinations are negligible and that the normalized probabilities for '1', '2' and '3' are 0.34, (0.11 + 0.04) and 0.03, respectively. This compares reasonably well to the measured values taken from Figure 4.4 which are '1'/'0' = 0.36, '2'/'0' = 0.19 and '3'/'0' = 0.05 (all ±0.01). Given that the sample has a gradient in the enrichment [26], the numbers can be considered to agree well.

Energy shifts of LVM satellites Tables 4.1 and 4.2 list positions and FWHM as well as shifts of all observed features in the S^+ $1s(T_2)$ spectra discussed here. The determined shifts can be compared to data given by Pajot et al. in [11] for ^{nat}Si. The L_3, L_2, L_1, H_1 shifts given there for Γ_7 are (in cm^{-1}) −0.807, −0.557, −0.274, +0.557 and for Γ_8 −0.968, −0.678, −0.355, +0.476. Within an error of approximately ±5 % these values are comparable to the ones determined with our samples.

As discussed earlier, the ^{30}Si sample shows a satellite pattern that is opposite to the ^{nat}Si pattern. As a consequence the shifts are positive. When comparing the corresponding values for ^{30}Si and ^{nat}Si given in Table 4.2 it is apparent that, within a margin of error, the magnitude of the shift is the same as for ^{nat}S.

Isotope broadening

^{28}Si:^{nat}S and ^{28}Si:^{34}S Now we will discuss the S^+ $1s(T_2)$ spectra of two different samples, ^{28}Si:^{nat}S and ^{28}Si:^{34}S shown in Figures 4.5 and 4.6. Overlays of enriched and natural silicon samples are shown in Figures 4.7 and 4.8, impressively exhibiting the broadening effect. Due to the elimination of isotope broadenings imposed by natural silicon we are now able to confirm some of the previously made assumptions on the origin of the absorption lines. We also see a dramatic sharpening of both transitions, especially in the lower energy $\Gamma_6 \rightarrow \Gamma_7$ transition. The stronger sharpening of the Γ_7 transition is also responsible for the reversal of the peak intensity ratio of the two components in ^{28}Si. The area underneath the transition line remains the same, causing an increase in intensity for narrow lines at high resolution. This can be easily seen in the overlay shown in Figure 4.8.

As outlined in Section 2.2 the significant broadening of absorption transition lines in silicon is due to the isotopic randomness present in $^{\mathrm{nat}}$Si. By using highly enriched ^{28}Si this random distribution of isotopes can be eliminated and the inhomogeneous broadening removed. We are then often left with homogeneous broadening due to the lifetime of the excited state, indicated by a Lorentzian line shape.

It was found that the ^{28}Si:$^{\mathrm{nat}}$S sample shown in Figure 4.5 is not strain free since the S^+ $1s(T_2)$ Γ_8 transition exhibits a small splitting with a peak separation of $0.006\,\mathrm{cm}^{-1}$ (see Section 2.1 and [13]). This is probably due to the heavy erosion on the specimen's surface. Polishing and etching has to be done very carefully not to reduce the sample's size even further and it seems that it was not carried out thoroughly enough here. To clear any doubts about the origin of the splitting, another sample, ^{28}Si:^{34}S was produced. The quality of this sample surpasses the previous one and it is here where we measure the record linewidth. A high resolution spectrum of S^+ $1s(T_2)$ of ^{34}S in ^{28}Si is shown in Figure 4.6. In this spectrum we measure a FWHM of only $0.008\,\mathrm{cm}^{-1}$ for the $1s(T_2)$ Γ_7 line and $0.022\,\mathrm{cm}^{-1}$ for the Γ_8 absorption line. The Γ_7 transition is, together with Se in ^{28}Si [35] the narrowest donor or acceptor absorption line observed in silicon to date – it is 22 times narrower than in previous S spectra [11] and narrower than P and B absorption transition lines in ^{28}Si by a factor of two [9]. This exceptional result can be explained by the fact that the $1s(A_1) \rightarrow 1s(T_2)$ transition is EMT forbidden but symmetry allowed and thus has a long radiative lifetime. At 1.5 K curve fitting indicates that the Γ_7 transition has a 100 % Lorentzian shape. Given the weakness of the transition line this number has to be considered carefully, nevertheless

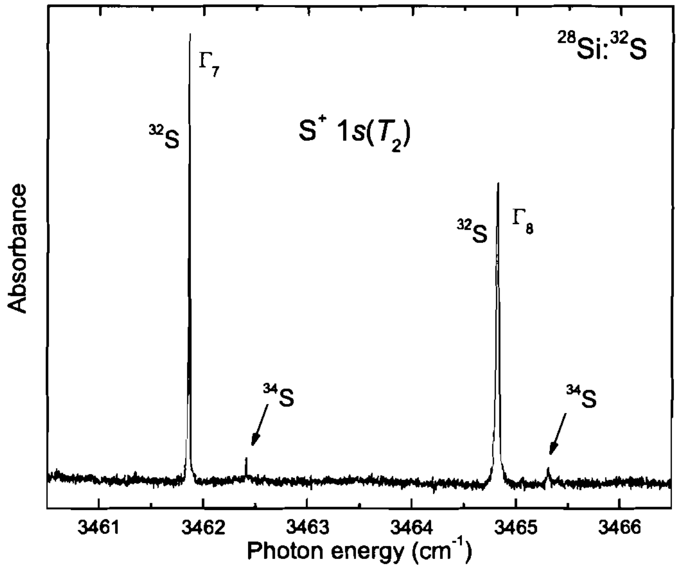

Figure 4.5: Fine structure of S^+ $1s(T_2)$ in ^{28}Si with a resolution of $0.0024\,\mathrm{cm}^{-1}$ and a temperature of 1.5 K. The satellites due to the Si isotope effect are eliminated and the energy shift between ^{32}S and ^{34}S centres is clearly visible.

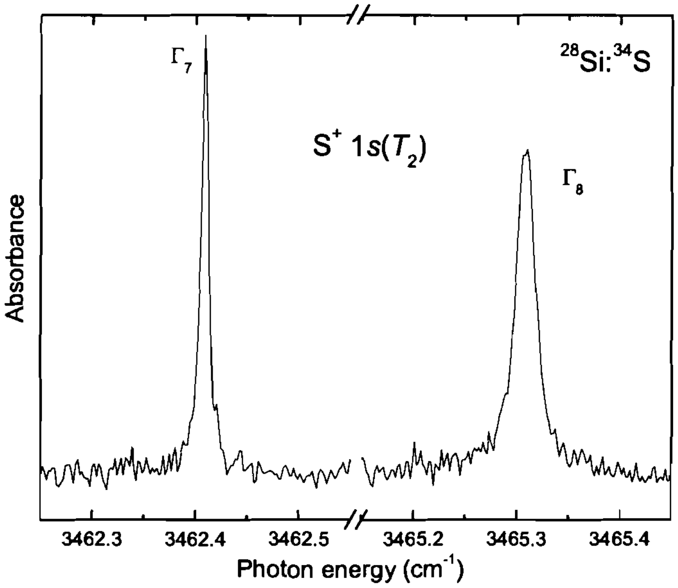

Figure 4.6: Detailed fine structure of $^{34}S^+$ $1s(T_2)$ absorption lines in ^{28}Si with a resolution of $0.0024\,\mathrm{cm}^{-1}$ and a temperature of 1.5 K. The FWHM of the $1s(T_2)$ Γ_7 absorption line is only $0.008\,\mathrm{cm}^{-1}$ and $0.022\,\mathrm{cm}^{-1}$ for the $1s(T_2)$ Γ_8 line.

it shows that the FWHM is lifetime limited. Γ_8 is only 88 % Lorentzian. In an experiment at 4.2 K the FWHM of Γ_7 increased by 60 % but kept its Lorentzian shape, while Γ_8 increased by only 20 %. At elevated temperatures thermally activated transitions reduce the lifetime of Γ_7 and thus increase the linewidth.

The energies measured for the $^{34}S^+$ $1s(T_2)$ absorption line in this sample correspond very well to those found for ^{34}S in the sample doped with ^{nat}S, given that the ^{34}S features there are rather weak. This can be seen in Figure 4.6 and also in Table 4.2.

Isotope shifts

Silicon host isotope shift In the overlay shown in Figure 4.7 it is clearly visible that a change in the host isotope composition not only gives rise to the satellites discussed earlier, but also introduces a shift to the binding energy. As discussed in Section 2.3.1 the impurity binding energy E_B increases with increasing host isotopic mass and therefore we see the absorption transition of S in ^{30}Si above the one in ^{nat}Si and ^{28}Si.

With the transition energies given in Tables 4.1 and 4.2 we can determine the energy shifts between the ^{28}Si, ^{nat}Si and ^{30}Si samples. For the '0' line of ^{32}S we find the values listed in Table 4.3. In principle we would expect a larger shift for the higher excited state, but since Γ_7 and Γ_8 are rather close together the energy shifts should be nearly identical like in our measurements.

Sulfur impurity isotope shift In Section 2.3.2 the impurity mass dependent energy shift was introduced. This impurity isotope shift has been shown in [21, 22], in particular in [7] for boron. In the case of the acceptor boron, the heavier isotope ^{11}B has a lower binding energy than the lighter ^{10}B, thus we see the absorption lines of ^{11}B at a lower energy than those of ^{10}B. However, for the S^+ $1s(T_2)$ transition we observe that the ^{32}S-associated absorption line is at lower energy than the one of ^{34}S. The difference $^{34}S - {}^{32}S$ in Table 4.2 is thus positive ($+0.555\,\mathrm{cm}^{-1}$ and $+0.495\,\mathrm{cm}^{-1}$). As explained we would normally expect this shift to be the same for both transitions, Γ_7 and Γ_8. However we measure a difference of approximately 10 % in between the shifts.

Table 4.2: Positions and FWHM of the components of S^+ $1s(T_2)$ Γ_7 and Γ_8 in various samples (in cm^{-1}). See Table 4.1 for ^{30}Si. Shifts are given with respect to '0' of the same spectrum, except ‡, which is with respect to '0'($^{\mathrm{nat}}$S) in ^{28}Si. Accuracy: ±0.020, * denotes transitions with > 90 % Lorentzian lineshape, † indicates reduced accuracy.

			Γ_7		
	L_3	L_2	L_1	0	H_1
^{28}Si:$^{\mathrm{nat}}$S	-	-	-	*3461.858	3462.413
FWHM	-	-	-	0.010	0.012
shift	-	-	-	0.000	+0.555
^{28}Si:^{34}S	-	-	-	*3462.409	-
FWHM	-	-	-	0.008	-
shift	-	-	-	‡+0.551	-
$^{\mathrm{nat}}$Si:$^{\mathrm{nat}}$S	3461.184	3461.445	3461.709	3461.986	3462.555
FWHM	-	0.157	0.134	0.157	0.197
shift	−0.802	−0.541	−0.277	0.000	+0.569
$^{\mathrm{nat}}$Si:^{34}S	†3461.730	3462.014	3462.266	3462.555	-
FWHM	-	0.196	0.155	0.196	-
shift	−0.825	−0.541	−0.289	0.000	-

			Γ_8		
	L_3	L_2	L_1	0	H_1
^{28}Si:$^{\mathrm{nat}}$S	-	-	-	3464.819	3465.314
FWHM	-	-	-	0.030	0.030
shift	-	-	-	0.000	+0.495
^{28}Si:^{34}S	-	-	-	*3465.308	-
FWHM	-	-	-	0.022	-
shift	-	-	-	‡+0.489	-
$^{\mathrm{nat}}$Si:$^{\mathrm{nat}}$S	†3464.014	3464.275	3464.590	3464.948	3465.465
FWHM	-	0.164	0.184	0.172	0.164
shift	−0.934	−0.673	−0.358	0.000	+0.517
$^{\mathrm{nat}}$Si:^{34}S	-	3464.795	3465.110	3465.457	-
FWHM	-	0.220	0.242	0.208	-
shift	-	−0.662	−0.347	0.000	-

Table 4.3: Silicon isotope shifts of the '0'-line of the S^+ $1s(T_2)$ transition All numbers in cm^{-1}.

	$^{28}Si-^{nat}Si$	$^{30}Si-^{nat}Si$	$^{30}Si-^{28}Si$
S^+ $1s(T_2)$ Γ_7	$-0.128\,cm^{-1}$	$0.444\,cm^{-1}$	$0.572\,cm^{-1}$
S^+ $1s(T_2)$ Γ_8	$-0.129\,cm^{-1}$	$0.422\,cm^{-1}$	$0.551\,cm^{-1}$

This could be related to the unusual sulfur isotope shift of the S^+ $1s(T_2)$ transition, as explained by Pajot et al. [11].

For shallow impurities like boron, only the ground state undergoes an impurity mass dependent isotope shift, while the excited states all remain at the same energy. The sulfur p-states and S^0 $1s(T_2)$ show the same sign of the shift as shallow impurities do. In contrast, the S^+ $1s(T_2)$ state is very deep and strongly localized. As explained in [11] this can lead to a reversed isotope shift of the $1s(T_2)$ excited state. This is not the case for S^+ p-states (Section 4.1.2) and also not for S^0 $1s(T_2)$ (Section 4.2.1).

4.1.2 S^+ p-states

In our samples the S^+ p-states are barely observed. One reason is that our samples have a relatively low boron concentration. A higher boron acceptor concentration would increase the degree of ionization of the sulfur impurity centres. Additionally the sulfur concentration in our samples is low, to ensure that the much sharper $1s(T_2)$ transitions do not saturate. We did not work extensively towards improving the S^+ p-state spectrum since the main attention was focused on the more than two orders of magnitude sharper $1s(T_2)$ transition. Besides the $2p_\pm$ absorption transition shown in Figure 4.9 for four different samples, only the $^{nat}Si{:}^{nat}S$ sample shows some of the weaker features. Those are the S^+ transitions $2p_0$ ($4581.52\,cm^{-1}$), $2s(T_2)$ ($4622.23\,cm^{-1}$), $3p_0$, $4p_0$, $3p_\pm$, $4p_\pm$ and $5p_\pm$. In [11] we find the values $4581.47\,cm^{-1}$ for $2p_\pm$ and $4622.68\,cm^{-1}$ for $2s(T_2)$. Given the signal to noise ratio in our spectrum these numbers agree well with our results. Table 4.4 gives a summary of the positions, FWHMs and respective Si or S isotope shifts of the S^+ $2p_\pm$ absorption line in

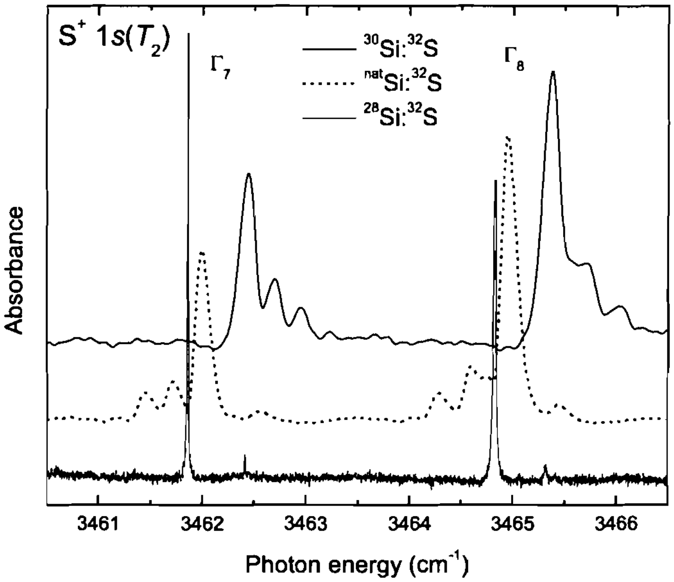

Figure 4.7: Energy shifts of S^+ $1s(T_2)$ due to different Si host isotope compositions. Due to the stronger sharpening of the $1s(T_2)$ Γ_7 transition, the Γ_7/Γ_8 intensity ratio is reversed in ^{28}Si. All spectra were recorded at a temperature of 1.5 K with a resolution of 0.004 cm^{-1} (^{28}Si), 0.050 cm^{-1} (^{30}Si) and 0.100 cm^{-1} (^{nat}Si).

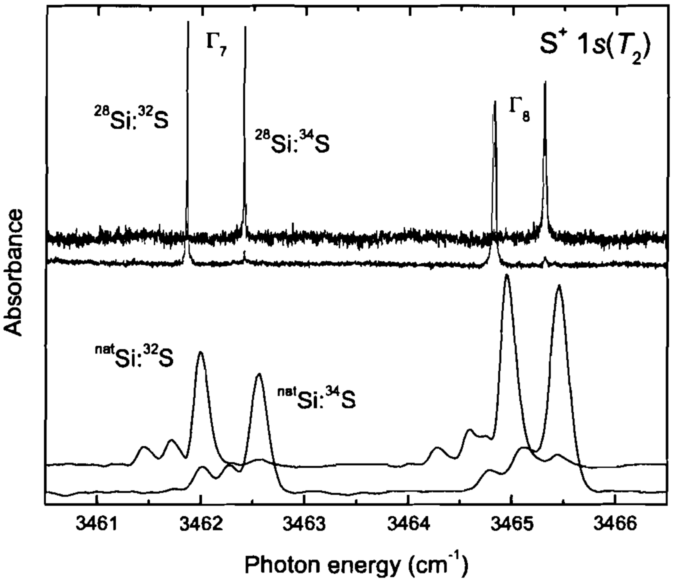

Figure 4.8: Energy shifts of S^+ $1s(T_2)$ due to different S dopant isotope compositions. The main peak of the ^{34}S spectrum superimposes with H_1 of the ^{32}S spectrum. All spectra were recorded at a temperature of 1.5 K with a resolution of 0.100 cm^{-1}.

our different samples. In all samples the absorption lines have a Lorentzian broadening, indicating that their FWHM is lifetime limited. In fact no significant difference in the FWHM in between the ^{28}Si and $^{\mathrm{nat}}$Si samples can be determined. As described earlier, the impurity isotope shift has the sign as predicted for S^+ p-states with the ^{34}S binding energy being lower than the one of the ^{32}S centre. This confirms a previously published result [14]. It should also be noted that the three S^+ $2p_\pm$ lines in $^{\mathrm{nat}}$Si and ^{30}Si shown in Figure 4.9 appear to have some unresolved structure on the high energy side. We also observe this for the Se^+ $2p_\pm$ transition where the splitting is clearly resolved [35].

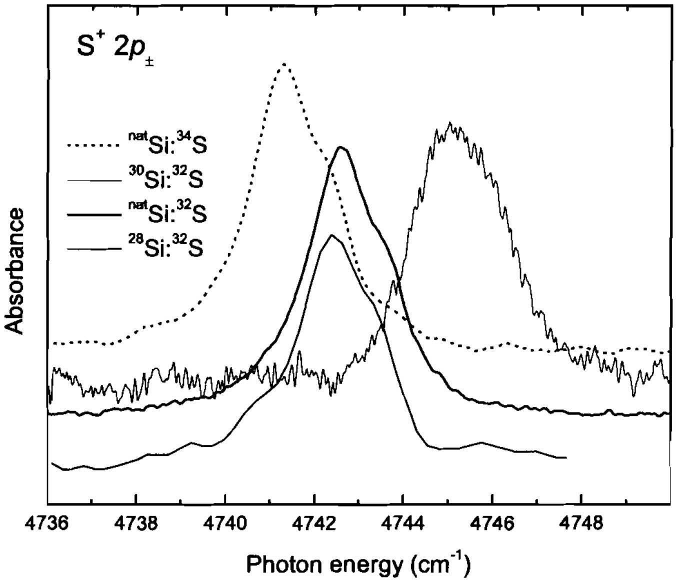

Figure 4.9: S^+ $2p_\pm$ in four different samples. Both the host (Si) and impurity (S) isotope shift are present. All spectra were recorded at a temperature of 1.5 K with a resolution of 0.500 cm^{-1} or better.

Table 4.4: Positions, FWHM and respective isotope shift of the S^+ $2p_\pm$ absorption line (with respect to ^{nat}Si:^{nat}S) in four different samples. All numbers in cm^{-1}.

S^+ $2p_\pm$	pos.	FWHM	Si-shift	^{34}S−^{32}S
^{nat}Si:^{nat}S	4742.687	2.02	0	-
^{28}Si:^{nat}S	4742.499	2.16	−0.19	-
^{30}Si:^{nat}S	4745.296	2.37	+2.61	-
^{nat}Si:^{34}S	4741.276	2.29	-	−1.41

4.2 The S^0 transitions

In the case of S^0 transitions one of the excess electrons of the sulfur centre remains in the ground state while the other one is involved in an absorption transition. In the following the $1s(A_1)$ grouns state to $1s(T_2)$ and p-state transitions of S^0 centres are discussed.

4.2.1 S^0 $1s(T_2)$ isotope effects

In Figure 4.10 the S^0 $1s(T_2)$ transition is shown for various samples. The spectra again show both effects, the silicon host isotope shift as well as the sulfur impurity isotope shift. The strong shoulders in ^{nat}Si and ^{30}Si suggest that the absorption lines might have unresolved satellites due to local vibrational modes comparable to those of S^+ $1s(T_2)$. Table 4.5 lists the relevant numbers of transition energies, FWHM and isotope shifts. Within a small margin of error the silicon isotope shifts are $(-0.147 \pm 0.001)\,\mathrm{cm}^{-1}$ for ^{nat}Si – ^{28}Si and $(1.665 \pm 0.013)\,\mathrm{cm}^{-1}$ for ^{30}Si – ^{nat}Si. The sulfur shift between ^{34}S and ^{32}S in ^{nat}Si and ^{28}Si is $(-0.606 \pm 0.002)\,\mathrm{cm}^{-1}$. The ^{30}Si sample shows a slightly smaller separation of $-0.59\,\mathrm{cm}^{-1}$ but the low signal to noise ratio for ^{34}S in ^{30}Si does not allow for any further conclusions here. It is expected that the shifts are the same (Section 2.3.2).

The isotope broadening effect is clearly visible and the linewidths are significantly narrower in ^{28}Si. The absorption line of ^{34}S in ^{28}Si:^{34}S has a width of $0.024\,\mathrm{cm}^{-1}$ and the fitting routine indicates that its shape is 100 % Lorentzian, reflecting that the FWHM is dominated by homogeneous lifetime broadening. The FWHM of S^+

Table 4.5: Positions, FWHM and isotope shifts of S^0 $1s(T_2)$ in various samples (in cm^{-1}). Silicon isotope shifts are given with respect to the ^{nat}Si:^{nat}S sample; sulfur isotope shifts are measured within the sample. Accuracy: ±0.020, * denotes transitions with ~ 100 % Lorentzian lineshape.

S^0 $1s(T_2)$	^{34}S	^{33}S	^{32}S	$^{34}S-^{32}S$
^{28}Si:^{nat}S	2287.632	-	*2288.240	−0.608
FWHM	0.05	-	0.047	-
Si-shift	−0.147	-	−0.145	-
^{28}Si:^{34}S	*2287.631	2287.926	2288.238	−0.607
FWHM	0.024	0.027	0.03	-
Si-shift	−0.148	-	−0.147	-
^{nat}Si:^{nat}S	2287.779	-	2288.385	−0.606
FWHM	0.15	-	0.210	-
Si-shift	0.000	-	0.000	-
^{nat}Si:^{34}S	2287.774	-	2288.377	−0.60
FWHM	0.143	-	0.16	-
Si-shift	-	-	-	-
^{30}Si:^{nat}S	2289.453	-	2290.041	−0.59
FWHM	0.31	-	0.227	-
Si-shift	1.674	-	1.656	-

$1s(T_2)$ Γ_7 is only one third of this value. Due to the strong shoulders in many of these absorption lines a side peak had to be used to achieve a reasonable fit function and the given FWHM thus shows the width of the main peak.

Figure 4.11 shows in greater detail ^{28}Si diffused either with ^{nat}S or with ^{34}S. The observed small peak due to ^{33}S in the ^{28}Si:^{34}S sample lies half-way in between the ^{34}S and ^{32}S peaks, within the given accuracy. It is also interesting to see that the enrichment of ^{34}S obviously also led to an enrichment of the other heavier isotopes, especially of ^{36}S. This isotope has a natural abundance of only 0.02 % and thus most likely would not be observable for natural silicon. Even though the feature in the spectrum attributed to ^{36}S is extremely weak it allows us to estimate the isotopic abundance of ^{36}S in this sample. With the help of the peak areas determined using a fit function we obtain the isotopic distribution shown in Table 4.6. Hence we are able to verify that the ~95 % enrichment of ^{34}S exceeds the supplier's specification

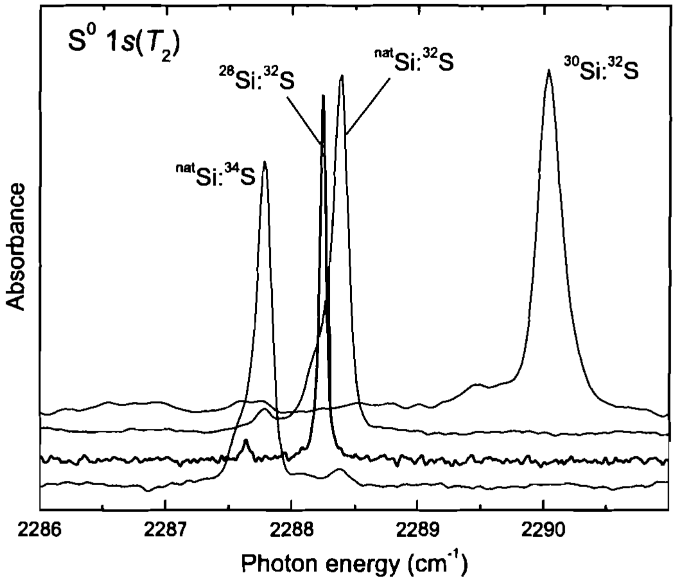

Figure 4.10: S^0 $1s(T_2)$ in four different samples. Both, the host (Si) and impurity (S) isotope shift are present. All spectra were recorded at a temperature of 1.5 K with resolutions of less than 0.100 cm^{-1} (0.020 cm^{-1} for ^{28}Si).

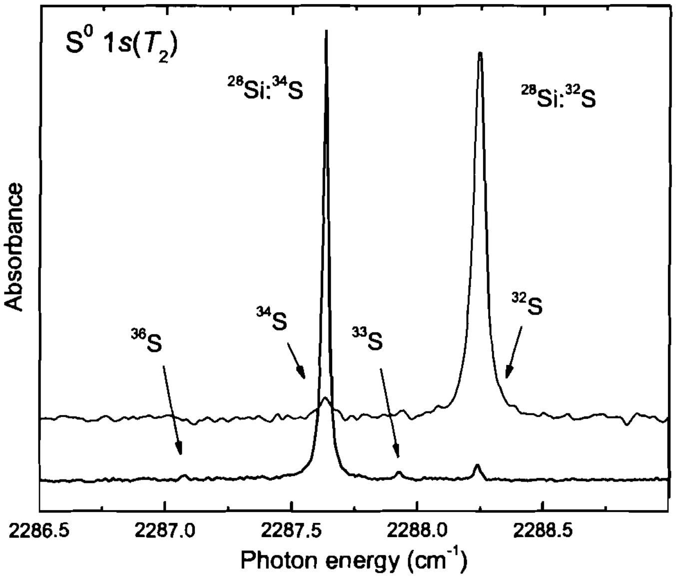

Figure 4.11: S^0 $1s(T_2)$ in ^{28}Si:$^{\mathrm{nat}}$S and ^{28}Si:^{32}S showing increased detail. In the enriched ^{34}S sample the isotopes ^{33}S and even ^{36}S are present. Both spectra were recorded at a temperature of 1.5 K with a resolution of 0.020 cm^{-1}.

and that ^{36}S has a concentration of about 0.8 %.

Table 4.6: Determined isotope enrichment of the ^{28}Si:^{34}S sample

	^{36}S	^{34}S	^{33}S	^{32}S
S^0 $1s(T_2)$ position in ^{28}Si (cm^{-1})	2287.074	2287.631	2287.926	2288.238
enrichment	0.8 %	94.6 %	1.4 %	3.1 %

4.2.2 S^0 *p*-states

Much has been reported about S^0 p-states in the past [10–12]. The essential features of the S p-states are very similar to those observed for shallow group V donors like P [10, 36]. We will compare our numbers with the ones published and have a closer look at the S^0 $2p_\pm$ transition. Figure 4.12 shows the p-states of ^{nat}Si and ^{28}Si. The chemical purity of ^{nat}Si is superior and thus we see more highly excited states in these samples. Figure 4.13 shows the high energy end of the ^{nat}Si spectrum in greater detail starting at $4p_\pm$ and the highest observed transition is $7h_\pm$. That is two highly excited state transitions more than shown in previously published results for S^0 [10–12, 37]. Absorption transitions up to $6p_\pm$ can be observed in the ^{28}Si sample. In both samples the S isotope splitting is visible for the $2p_0$ and $2p_\pm$ transitions. Labels were assigned with the help of data given in [12] for S^0 and in [10] for S_2^0 (this data had to be scaled to low energy S^0 transitions). Table 4.7 gives an overview of absorption line positions and FWHM in four different samples, while Table 4.8 lists the energy shifts due to the sulfur and silicon isotope effects. The sulfur isotope shift between the samples doped with ^{nat}S and ^{34}S fluctuates around $(0.646\pm0.020)\,\mathrm{cm}^{-1}$. As described in Section 2.3.2 a constant shift throughout a spectrum in between the absorption lines of different impurity isotopes is expected.

In contrast to this we observe an increasing shift in energy in between the different silicon isotopes for higher excited states, similar to B and P absorption transitions [8, 9]. As outlined in Section 2.3.1, the dependence of ϵ_0 and m^* on the isotopic mass scales the ground state and excited state binding energies by an identical factor, and thus the largest shifts are observed for transitions to the highest excited states.

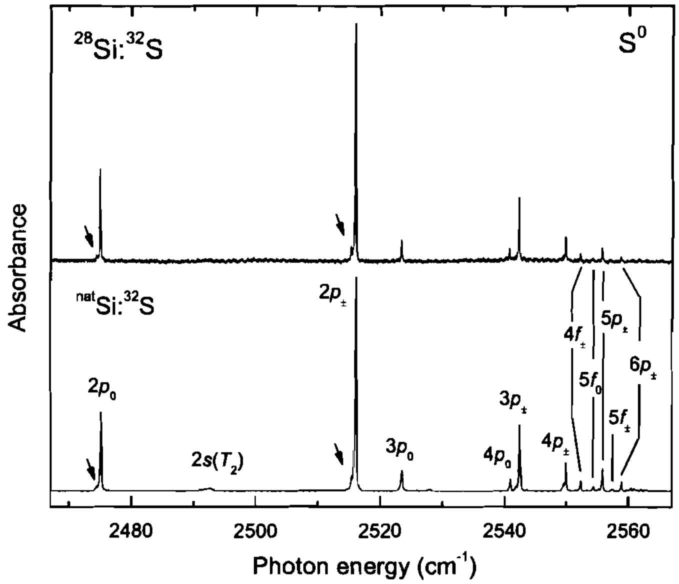

Figure 4.12: S^0 p-states for ^{nat}Si (bottom) and ^{28}Si (top) diffused with ^{nat}S. Labels are attached to the transition lines present in ^{28}Si. The arrows indicate absorption lines due to ^{34}S impurity centres wherever they are strong enough to be observed. The high-energy end of the ^{nat}Si spectrum can be seen in more detail in Figure 4.13. All spectra were recorded at a temperature of 1.5 K with a resolution of 0.050 cm^{-1}.

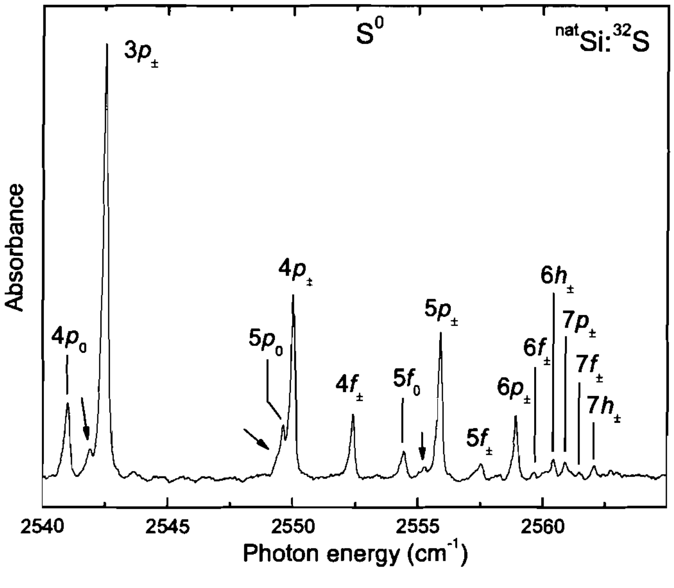

Figure 4.13: High energy S^0 p-states in ^{nat}Si diffused with ^{nat}S at a temperature of 1.5 K with a resolution of 0.050 cm^{-1}. The arrows indicate absorption lines due to ^{34}S impurity centres wherever they are strong enough to be observed.

Table 4.7: Positions (first line) and FWHM (second line) of S^0 p-states in various samples (in cm^{-1}). Corresponding isotope shifts are in listed in Table 4.8. Accuracy: ±0.020, † indicates reduced accuracy.

	$^{nat}Si{:}^{nat}S$		$^{28}Si{:}^{nat}S$		$^{30}Si{:}^{nat}S$		$^{nat}Si{:}^{34}S$	
	^{32}S	^{34}S	^{32}S	^{34}S	^{32}S	^{34}S	^{32}S	^{34}S
$2p_0$	2475.123	2474.473	2474.967	2474.319	2477.019	-	2475.091	2474.463
	0.174	0.168	0.112	-	0.261	-	0.118	0.202
$2s(T_2)$	†2492.40	-	-	-	-	-	-	-
$2p_\pm$	2516.039	2515.423	2515.870	2515.243	2517.979	-	2516.019	2515.397
	0.182	0.277	0.125	0.194	0.276	-	0.160	0.205
$3p_0$	2523.466	-	2523.315	-	2525.392	-	-	2522.827
	0.289	-	0.172	-	-	-	-	0.259
$4p_0$	2540.971	-	2540.819	-	2542.931	-	-	2540.322
	0.262	-	0.150	-	0.269	-	-	0.252
$3p_\pm$	2542.506	2541.869	2542.338	†2541.70	2544.448	†2543.84	†2542.48	2541.843
	0.175	0.193	0.147		0.265	-	-	0.206
$5p_0$	2549.596	-	-	-	-	-	-	2549.912
	0.260	-	-	-	-	-	-	†0.25
$4p_\pm$	2549.998	2549.370	2549.833	2549.400	2551.942	-	2549.997	2549.351
	0.161	-	0.112	0.197	0.282	-	-	0.162
$4f_\pm$	2552.362	-	2552.199	-	2554.304	-	-	2551.721
	0.206	-	0.168	-	0.169	-	-	0.182
$5f_0$	2554.388	-	-	-	-	-	-	2553.755
	0.274	-	-	-	-	-	-	0.237
$5p_\pm$	2555.888	2555.245	2555.719	-	2557.836	-	-	2555.241
	0.199	0.317	0.151	-	0.288	-	-	0.168
$5f_\pm$	2557.454	-	-	-	-	-	-	2556.846
	0.320	-	-	-	-	-	-	0.197
$6p_\pm$	2558.913	-	2558.744	-	2560.923	-	-	2558.271
	0.171	-	0.117	-	-	-	-	0.158
$6f_\pm$	2559.633	-	-	-	-	-	-	-
$6h_\pm$	2560.426	-	-	-	-	-	-	2559.765
$7p_\pm$	2560.913	-	-	-	-	-	-	2560.289
$7f_\pm$	2561.468	-	-	-	-	-	-	†2560.86
$7h_\pm$	2562.055	-	-	-	-	-	-	2561.407

Table 4.8: Isotope shifts of S^0 p-states in various samples (in cm^{-1}). Corresponding energies are listed in Table 4.7. Accuracy: ±0.020, † indicates reduced accuracy.

S^0	$^{28}Si-^{nat}Si$	$^{30}Si-^{nat}Si$	$^{34}S-^{32}S$
$2p_0$	−0.156	1.896	−0.660
$2p_\pm$	−0.169	1.940	−0.642
$3p_0$	−0.151	1.926	−0.639
$4p_0$	−0.152	1.960	−0.649
$3p_\pm$	−0.168	1.942	−0.663
$5p_0$	-	-	−0.684
$4p_\pm$	−0.165	1.944	−0.647
$4f_\pm$	−0.163	1.942	−0.641
$5f_0$	-	-	−0.633
$5p_\pm$	−0.169	1.948	−0.647
$5f_\pm$	-	-	−0.608
$6p_\pm$	−0.169	2.010	−0.642
$6f_\pm$	-	-	-
$6h_\pm$	-	-	−0.661
$7p_\pm$	-	-	−0.624
$7f_\pm$	-	-	†−0.61
$7h_\pm$	-	-	−0.648

In Table 4.9 our experimentally determined transition energies for the ^{nat}Si:^{nat}S sample are compared to previous publications. Published listings are not complete and thus not all values could be matched. For reference [10], energies from the S_2^0 transition had to be scaled to align with their values for S^0 and in the case of reference [12] some values were taken from the publication's list of theoretical EMT values. With few exceptions the deviation in general is only on the order of a tenth of a wavenumber with no significant trend. Those deviations can easily be caused by different sample qualities or degraded resolution. As discussed before, some of our peaks show relatively strong asymmetries that can contribute to a minor shift in the determined peak energy.

The S^0 $2p_\pm$ transition is the strongest one in this p-state spectrum and clearly present in every sample. We use this transition to have a closer look at the energy shifts due to sulfur and silicon isotope effects in Figure 4.14. We can see that the respective ^{32}S and ^{34}S peaks in natural silicon superimpose. The ^{32}S peak in ^{28}Si is shifted to lower energy, while the one in ^{30}Si is shifted to higher energy. The sharpening is not as strong as observed for the $1s(T_2)$ transitions but it is clearly visible. The ^{nat}Si and ^{30}Si samples also exhibit a tail on the low energy side for the first and on the high energy side for the latter. This is similar to the tails observed for phosphorus transitions in natural silicon [9].

Table 4.9: Comparison of the measured S^0 transition energies of the ^{nat}Si:^{nat}S sample to experimentally determined literature values. All energies are given in cm^{-1}. Values marked with ^{a} are taken from the S_2^0 spectrum in [10] and scaled while values with ^{b} are taken from the EMT calculation in [12]. † indicates reduced accuracy.

S^0	This Work	Ref. [10]	Ref. [12]
$1s(T_2)$	2288.385	-	2288.61
$2p_0$	2475.123	-	2475.12
$2s(T_2)$	†2492.4	-	2493.34
$2p_\pm$	2516.039	-	2516.15
$3p_0$	2523.466	-	2523.73
$3s$	-	-	2528.32
$4p_0$	2540.971	-	2540.97
$3p_\pm$	2542.506	2542.42	2542.51
$5p_0$	2549.596	2549.63	-
$4p_\pm$	2549.998	2549.92	2550.00
$4f_\pm$	2552.362	2552.25	2552.26
$5f_0$	2554.388	2554.37	2554.35
$5p_\pm$	2555.888	2555.78	2555.89
$5f_\pm$	2557.454	-	2557.34
$6h_0$	-	-	^{b}2558.77
$6p_\pm$	2558.913	2558.82	2558.95
$6f_\pm$	2559.633	-	^{b}2559.58
$6h_\pm$	2560.426	2560.36	^{b}2560.51
$7p_\pm$	2560.913	-	2561.04
$7f_\pm$	2561.468	^{a}2561.43	-
$7h_\pm$	2562.055	^{a}2561.99	-

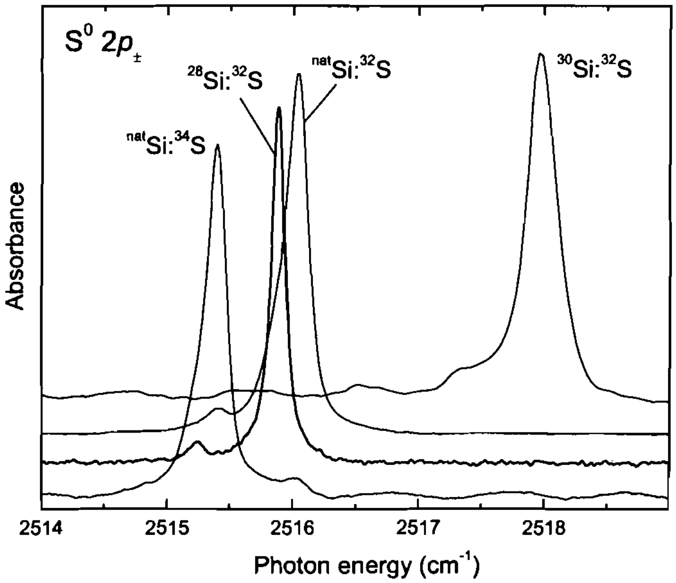

Figure 4.14: S^0 $2p_\pm$ in four different samples. Both the host (Si) and impurity (S) isotope shift are present. All spectra were recorded at a temperature of 1.5 K with a resolution of $0.100\,\mathrm{cm}^{-1}$.

4.3 The S_2^0 transitions

Our samples were prepared in a way to keep the amount of S_2 pair formation to a minimum. Hence we generally do not observe strong absorption lines due to sulfur pairs. Nevertheless the $2p_\pm$ transition is strong enough in all samples to obtain values for position and width of the absorption line (Table 4.10). The data shown here is the first available information on isotope effects on the S_2^0 transition. Figure 4.15 shows the $2p_\pm$ lines in our samples. It is apparent that the host isotope enrichment has a fairly small influence on the linewidth, which must be limited by lifetime broadening. The sharpening is by far less dramatic than for the $1s(T_2)$ transitions, but comparable to that of the S^+ and S^0 $2p_\pm$ transitions.

Table 4.10: Position (first line), FWHM (second line) and respective isotope shift of the S_2^0 $2p_\pm$ absorption line in four different samples. Si shift with respect to ${}^{nat}Si{:}{}^{nat}S$. All numbers in cm^{-1}.

S_2^0 $2p_\pm$	${}^{34}S$	${}^{32}S$	Si-shift	${}^{34}S-{}^{32}S$
${}^{nat}Si{:}{}^{nat}S$	-	1461.809	-	-
	-	0.280	-	-
${}^{28}Si{:}{}^{nat}S$	1460.98	1461.736	−0.073	−0.756
	-	0.180	-	-
${}^{30}Si{:}{}^{nat}S$	-	1462.697	−0.888	-
	-	0.304	-	-
${}^{nat}Si{:}{}^{34}S$	1461.211	-	-	-
	0.303	-	-	-

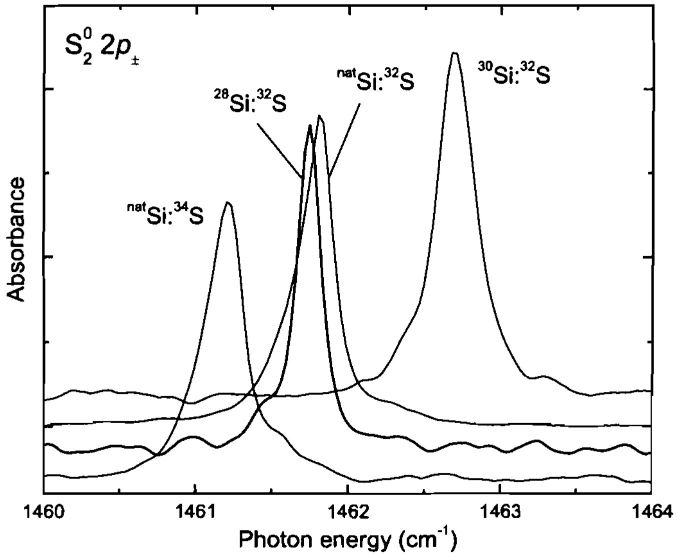

Figure 4.15: S_2^0 $2p_\pm$ in four different samples. Both, the host (Si) and impurity (S) isotope shift are present. All spectra were recorded at a temperature of 1.5 K with a resolution of 0.100 cm^{-1}.

Chapter 5

Conclusions

In this thesis spectroscopy on the deep double donor sulfur in isotopically enriched and natural silicon was done. Special samples were prepared for this purpose. Here we present new results regarding isotope effects in enriched ^{28}Si and ^{30}Si, showing several different isotope effects. We can identify satellite peaks at the S^+ $1s(T_2)$ transition as a result of different local vibrational modes of the Si_4 cluster surrounding the impurity centre, confirming published literature [11]. We observe the impurity isotope dependent energy shift due to the shift in zero point energy of the local vibrational mode of the sulfur impurity centre, verifying previous publications regarding S^+ p-states [14] and the S^+ $1s(T_2)$ transition [11]. The samples also exhibit an energy shift depending on the host isotope enrichment. The quality of the samples allowed us to measure the sharpest absorption transition line ever seen in a semiconductor, the S^+ $1s(T_2)$ Γ_7 transition, where we measured a full width at half maximum of only $0.008\,\mathrm{cm}^{-1}$, a factor of 22 narrower than in $^{\mathrm{nat}}$Si. In addition to that we report on host and impurity isotope shifts of the S_2^0 absorption transitions for the first time and we observe two more highly excited S^0 p-states in $^{\mathrm{nat}}$Si than reported before.

While our experiment was focussed on this $1s(T_2)$ transition, it also improves upon previously published literature in other aspects. The obtained data was compared to literature values and found to be in excellent agreement.

Bibliography

[1] K. Nishikawa and R. Barrie. *Phonon broadening of impurity spectral lines. I. General theory.* Can. J. Phys., **41**:1135 (1963).

[2] R. Barrie and K. Nishikawa. *Phonon broadening of impurity spectral lines. II. Application to silicon.* Can. J. Phys., **41**:1823 (1963).

[3] D. Karaiskaj, M. L. W. Thewalt, T. Ruf, M. Cardona, H.-J. Pohl, G. G. Deviatych, P. G. Sennikov and H. Riemann. *Photoluminescence of Isotopically Purified Silicon: How Sharp are Bound Exciton Transitions?* Phys. Rev. Lett., **86**(26):6010–6013 (2001).

[4] M. L. W. Thewalt and D. M. Brake. Mater. Sci. Forum, **65–66**:187 (1990).

[5] M. L. W. Thewalt, T. A. Meyer, D. Karaiskaj, M. Cardona, E. E. Haller, J. W. Ager and H. Riemann. *Progress in Semiconductor Spectroscopy Using Isotopically Enriched Si.* In J. Menéndez and C. G. van de Walle, editors, *AIP Conf. Proc. 772: Physics of Semiconductors*, pages 67–68 (2005).

[6] M. L. W. Thewalt. *Spectroscopy of excitons and shallow impurities in isotopically enriched silicon – electronic properties beyond the virtual crystal approximation.* Solid State Commun., **133**(11):715–725 (2005).

[7] D. Karaiskaj, J. A. H. Stotz, T. Meyer, M. L. W. Thewalt and M. Cardona. *Impurity Absorption Spectroscopy in ^{28}Si: The Importance of Inhomogeneous Isotope Broadening.* Phys. Rev. Lett., **90**(18):186402 (2003).

[8] D. Karaiskaj, T. A. Meyer, M. L. W. Thewalt and M. Cardona. *Dependence of the ionization energy of shallow donors and acceptors in silicon on the host isotopic mass.* Phys. Rev. B, **68**(12):121201 (2003).

[9] M. Steger, A. Yang, D. Karaiskaj, M. L. W. Thewalt, E. E. Haller, J. W. A. III, M. Cardona, H. Riemann, N. V. Abrosimov, A. V. Gusev, A. D. Bulanov, A. K. Kaliteevskii, O. N. Godisov, P. Becker, H.-J. Pohl and K. M. Itoh. *Shallow Impurity Absorption Spectroscopy in Isotopically Enriched Silicon.* In *AIP Conference*

Proceedings, 28th International Conference on the Physics of Semiconductors, Vienna - ICPS 2006, volume 893, pages 231–232 (2006).

[10] B. Pajot, G. Grossmann, M. Astier and C. Naud. *Higly Excited States of Donor Centres in Silicon.* Solid State Commun., **54**(1):57 (1985).

[11] B. Pajot, B. Clerjaud and M. D. McCluskey. *Isotope effects in the electronic spectrum of S^+ and Se^+ in silicon.* Phys. Rev. B, **69**(8):085210 (2004).

[12] E. Janzen, R. Stedman, G. Grossmann and H. G. Grimmeiss. *High-resolution studies of sulfur- and selenium-related donor centers in silicon.* Phys. Rev. B, **29**(4):1907–1918 (1984).

[13] H. G. Grimmeiss, E. Janzen and K. Larsson. *Multivalley spin splitting of 1s states for sulfur, selenium, and tellurium donors in silicon.* Phys. Rev. B, **25**(4):2627–2632 (1982).

[14] R. A. Forman. *Optical study of isotopic effects in the sulfur deep level in silicon.* Appl. Phys. Lett., **37**(9):776–778 (1980).

[15] R. A. Faulkner. *Higher Donor Excited States for Prolate-Spheroid Conduction Bands: A Reevaluation of Silicon and Germanium.* Phys. Rev., **184**(3):713–721 (1969).

[16] W. Kohn and J. M. Luttinger. *Theory of Donor States in Silicon.* Phys. Rev., **98**(4):915–922 (1955).

[17] C. Kittel and A. H. Mitchell. *Theory of Donor and Acceptor States in Silicon and Germanium.* Phys. Rev., **96**(6):1488–1493 (1954).

[18] P. J. Dean, R. A. Faulkner and S. Kimura. *Optical Properties of the Donor Tin in Gallium Phosphide.* Phys. Rev. B, **2**(10):4062–4076 (1970).

[19] H. Kim, A. K. Ramdas, S. Rodriguez and T. R. Anthony. *Electronic transitions of holes bound to boron acceptors in isotopically controlled diamonds.* Solid State Commun., **102**(12):861–865 (1997).

[20] M. Cardona. *Dependence of the excitation energies of boron in diamond on isotopic mass.* Solid State Commun., **121**(1):7–8 (2002).

[21] V. Heine and C. H. Henry. *Theory of the isotope shift for zero-phonon optical transitions at traps in semiconductors.* Phys. Rev. B, **11**(10):3795–3803 (1975).

[22] S. M. Kogan. *Isotopic shift of zero-phonon lines in spectra of shallow impurity centers in semiconductors.* Sov. Phys. - Semicond., **13**(10):1131–1134 (1979).

[23] P. Becker, D. Schiel, H.-J. Pohl, A. K. Kaliteevski, O. N. Godisov, M. F. Churbanov, G. G. Devyatykh, A. V. Gusev, A. D. Bulanov, S. A. Adamchik, V. A. Gavva, I. D. Kovalev, N. V. Abrosimov, B. Hallmann-Seiffert, H. Riemann, S. Valkiers, P. Taylor, P. D. Bièvre and E. M. Dianov. *Large-scale production of highly enriched* ^{28}Si *for the precise determination of the Avogadro constant.* Meas. Sci. Technol., **17**:1854–1860 (2006).

[24] A. Yang, M. Steger, D. Karaiskaj, M. L. W. Thewalt, M. Cardona, K. M. Itoh, H. Riemann, N. V. Abrosimov, M. F. Churbanov, A. V. Gusev, A. D. Bulanov, A. K. Kaliteevskii, O. N. Godisov, P. Becker, H.-J. Pohl, J. W. A. III and E. E. Haller. *Optical Detection and Ionization of Donors in Specific Electronic and Nuclear Spin States.* Phys. Rev. Lett., **97**(22):227401 (2006).

[25] M. L. W. Thewalt, A. Yang, M. Steger, D. Karaiskaj, M. Cardona, H. Riemann, N. V. Abrosimov, A. V. Gusev, A. D. Bulanov, I. D. Kovalev, A. K. Kaliteevskii, O. N. Godisov, P. Becker, H. J. Pohl, E. E. H. J. W. A. III and K. M. Itoh. *Direct observation of the donor nuclear spin in a near-gap bound exciton transition:* ^{31}P *in highly enriched* ^{28}Si*.* J. Appl. Phys., **101**(8):081724 (2007).

[26] J. W. Ager, III, J. W. Beeman, W. L. Hansen, E. E. Haller, I. D. Sharp, C. Liao, A. Yang, M. L. W. Thewalt and H. Riemann. *High-Purity, Isotopically Enriched Bulk Silicon.* J. Electrochem. Soc., **152**(6):G448–G451 (2005).

[27] F. Rollert, N. A. Stolwijk and H. Mehrer. *Diffusion of sulfur-35 into silicon using an elemental vapor source.* Appl. Phys. Lett., **63**(4):506–508 (1993).

[28] N. Sclar. *The effect of dopant diffusion vapor pressure on the properties of sulfur and selenium doped silicon infrared detectors.* J. Appl. Phys., **52**(8):5207–5217 (1981).

[29] *Landolt-Börnstein - Group III Condensed Matter*, volume 22b. Springer-Verlag (1997).

[30] R. C. Jaeger. *Introduction to Microelectronic Fabrication, second edition.* Prentice Hall (2002).

[31] A. A. Michelson. Phil. Mag., **31**(5):256 (1891).

[32] P. R. Griffiths and J. A. de Haseth. *Fourier Transform Infrared Spectroscopy.* John Wiley & Sons, Inc. (1986).

[33] J. K. Kauppinen, D. J. Moffatt, D. G. Cameron and H. H. Mantsch. *Noise in Fourier self-deconvolution.* Appl. Opt., **20**:1866 (1981).

[34] M. Steger, A. Yang, M. L. W. Thewalt, M. Cardona, H. Riemann, N. V. Abrosimov, M. F. Churbanov, A. V. Gusev, A. D. Bulanov, I. D. Kovalev, A. K. Kaliteevskii, O. N. Godisov, P. Becker, H.-J. Pohl, J. W. A. III and E. E. Haller. *Impurity Absorption Spectroscopy of the Deep Double Donor Sulfur in Isotopically Enriched Silicon.* In *International Conference on Defects in Semiconductors (ICDS-24), Albuquerque, NM* (2007).

[35] M. L. W. Thewalt, M. Steger, A. Yang, M. Cardona, H. Riemann, N. V. Abrosimov, M. F. Churbanov, A. V. Gusev, A. D. Bulanov, I. D. Kovalev, A. K. Kaliteevskii, O. N. Godisov, P. Becker, and H.-J. Pohl. *Well Resolved Hyperfine Structure in the Absorption Spectrum of* ^{77}*Se in Highly Enriched* ^{28}*Si.* In *International Conference on Defects in Semiconductors (ICDS-24), Albuquerque, NM* (2007).

[36] C. Jagannath, Z. W. Grabowski and A. K. Ramdas. *Linewidths of the electronic excitation spectra of donors in silicon.* Phys. Rev. B, **23**:2082 (1981).

[37] W. E. Krag, W. H. Kleiner and H. J. Zeiger. *Electronic structure of deep-lying sulfur centers in Si.* Phys. Rev. B, **33**(12):8304–8320 (1986).